



Targeting a lineage-specific PI3K –Akt signaling module in acute myeloid leukemia using a heterobifunctional degrader molecule

Lois Kelly, Justine Rutter, Kevin Lin, Frank Ling, Matthieu Duchmann, Emmanuelle Latour, Nadia Arang, Hélène Pasquer, Duong Ho Nhat, Juliette Charles, et al.

► To cite this version:

Lois Kelly, Justine Rutter, Kevin Lin, Frank Ling, Matthieu Duchmann, et al.. Targeting a lineage-specific PI3K –Akt signaling module in acute myeloid leukemia using a heterobifunctional degrader molecule. *Nature Cancer*, In press, Online ahead of print. 10.1038/s43018-024-00782-5 . hal-04598240

HAL Id: hal-04598240

<https://hal.science/hal-04598240v1>

Submitted on 6 Jun 2024

HAL is a multi-disciplinary open access archive for the deposit and dissemination of scientific research documents, whether they are published or not. The documents may come from teaching and research institutions in France or abroad, or from public or private research centers.

L'archive ouverte pluridisciplinaire **HAL**, est destinée au dépôt et à la diffusion de documents scientifiques de niveau recherche, publiés ou non, émanant des établissements d'enseignement et de recherche français ou étrangers, des laboratoires publics ou privés.

Targeting a Lineage-Specific PI3K γ /AKT Signaling Module in Acute Myeloid Leukemia Using a Heterobifunctional Degradar Molecule

Lois M. Kelly^{1,*}, Justine C. Rutter^{2,*}, Kevin H. Lin^{2,*}, Frank Ling¹, Matthieu Duchmann¹, Emmanuelle Latour¹, Nadia Arang^{3,4}, H       Pasquer¹, Duong Ho Nhat¹, Juliette Charles¹, Shane T. Killarney², Hazel X. Ang², Federica Namor¹, C       Culeux¹, B  rang     Lombard⁵, Damarys Loew⁵, Danielle L. Swaney^{3,4,9}, Nevan J. Krogan^{3,4,9}, Luc Brunel⁶,        Carretero⁶, Pascal Verdi  ⁶, Muriel Amblard⁶, Sofiane Fodil⁷, Tony Huynh⁷, Marie Sebert^{1,7}, Lionel Ad    ^{1,7}, Emmanuel Raffoux^{1,7}, Nina Fenouille¹, Rapha     Itzykson^{1,7}, Camille Lobry¹, Lina Benajiba^{1,8}, Antoine Forget^{3,4}, Anthony R. Martin^{6,#}, Kris C. Wood^{2,#}, and Alexandre Puissant^{1,#}.

¹ INSERM UMR 944, IRSL, St Louis Hospital, University of Paris-Cit  , Paris, France.

² Department of Pharmacology and Cancer Biology, Duke University, Durham, North Carolina.

³ Quantitative Biosciences Institute (QBI), University of California San Francisco, San Francisco, CA, USA.

⁴ Department of Cellular and Molecular Pharmacology, University of California San Francisco, San Francisco, CA, USA.

⁵ Curie Institute, PSL Research University, Mass Spectrometry and Proteomics facility, Paris, France.

⁶ IBMM, University of Montpellier, CNRS, ENSCM, Montpellier, France.

⁷ Department of Hematology and Immunology, H       Saint-Louis, AP-HP, Universit   Paris Cit  , Paris, France.

⁸ Universit   Paris Cit  , Clinical Investigation Center, Saint-Louis Hospital, Assistance Publique-H         de Paris (AP-HP), Paris, France.

⁹ Gladstone Institutes, San Francisco, California, USA.

* These authors contributed equally to this work.

These senior authors contributed equally to this work.

CORRESPONDING AUTHORS

Alexandre Puissant, *Ph.D.*: alexandre.puissant@inserm.fr

Kris C. Wood, *Ph.D.*: kris.wood@duke.edu

Anthony R. Martin, *Ph.D.*: anthony.martin@umontpellier.fr

SUMMARY

31 Dose-limiting toxicity poses a major limitation to the clinical utility of targeted cancer therapies,
32 often arising from target engagement in non-malignant tissues. This obstacle can be minimized
33 by targeting cancer dependencies driven by proteins with tissue- and/or tumor-restricted
34 expression. In line with another recent report, we show here that in acute myeloid leukemia (AML),
35 suppression of the myeloid-restricted PIK3CG/p110 γ -PIK3R5/p101 axis inhibits AKT signaling
36 and compromises AML cell fitness. Further, silencing PIK3CG/p110 γ or PIK3R5/p101 sensitizes
37 AML cells to established AML therapies. Importantly, we find that existing small molecule
38 inhibitors against PIK3CG are insufficient to achieve a sustained long-term anti-leukemic effect.
39 To address this concern, we developed a PROteolysis-TArgeting Chimera (PROTAC)
40 heterobifunctional molecule that specifically degrades PIK3CG and potently suppresses AML
41 progression alone and in combination with venetoclax in human AML cell lines, primary AML
42 patient samples, and syngeneic mouse models.

KEYWORDS

43 Acute Myeloid Leukemia (AML), Lineage-restricted Dependencies, PIK3CG/p110 γ ,
44 PIK3R5/p101, Venetoclax Synergistic Combination, AKT Signaling, PROteolysis TArgeting
45 Chimera (PROTAC) Degradar.

INTRODUCTION

Acute myeloid leukemia (AML) is a hematologic malignancy characterized by the clonal proliferation of abnormal myeloid progenitors in the bone marrow and peripheral blood. The five-year overall survival rate for patients diagnosed with *de novo* AML is 30%, with rates that exceed 50% in younger patients but are below 10% in patients diagnosed after the age of 60¹. This disparity is complex but at least partially driven by the inability of older patients to tolerate the highly toxic chemotherapies that have traditionally formed the cornerstone of first-line induction regimens. Given that AML is a disease of the elderly with a median age at diagnosis of 68, it is therefore responsible for significant cancer-related mortality². However, after decades of stagnation, a flurry of recent translational developments is now overturning this *status quo*. Since 2017, the United States Food and Drug Administration (FDA) has approved more than 10 new drugs for treating AML, several of which are first-in-class therapies designed to shut down specific, aberrantly-activated pathways¹. For example, AML driven by mutations in *FLT3*, *IDH1*, or *IDH2* can now be treated with small-molecule inhibitors that precisely target the mutated enzyme, abrogating downstream leukemogenic signaling³. Elderly patients ineligible for the standard 7+3 cytarabine- and daunorubicin-based chemotherapy are instead treated with the BCL2 inhibitor, venetoclax, combined with azacitidine or decitabine⁴. This regimen is significantly better tolerated in these patients compared to standard chemotherapy and has demonstrated improvement in overall survival among elderly AML patients⁵. Unfortunately, most patients diagnosed with AML lack actionable mutations, underscoring the need to identify additional therapeutic targets, ideally those that are agnostic to clinical subtype or mutational profile, and potentially inclusive of those entrenched deep within the cancer's identity.

A cancer's tissue-of-origin templates key features of its biology, implying that certain lineage-specific programs may be co-opted in neoplastic precursor cells to support tumorigenesis and tumor progression⁶. Consistent with this concept, a number of successful anticancer

therapies function by targeting lineage-specific survival factors⁷⁻¹⁰. This approach stands in contrast with most traditional targeted therapies, which engage targets that are ubiquitously expressed and are thus vulnerable to broad side effect profiles. Targeting nodes whose expression and/or function are unique to the cell lineage giving rise to malignancy provides an opportunity to effectively curb tumor survival while minimizing collateral damage in other tissues.

The effectiveness and tolerability of agents targeting lineage-restricted survival factors, which have ultimately been approved as anticancer therapies, are exemplified in hormone-responsive cancers such as receptor-positive breast and prostate cancers^{8,9}. In hematological malignancies, the potential of lineage-directed therapies is evidenced in the treatment of chronic lymphocytic leukemia (CLL), which has been transformed over the past decade by the introduction of multiple agents targeting dependencies specific to the B-cell lineage⁷. For instance, inhibitors of Bruton's tyrosine kinase (BTK), a B-cell restricted enzyme that relays essential cell survival and migration signals in CLL and other B-cell malignancies, induce durable remissions in CLL patients¹¹. Importantly, BTK inhibitors like ibrutinib are widely tolerable, with a narrow side effect profile that is consistent with BTK's restricted expression, therefore permitting chronic use.

Phosphoinositide 3-kinase (PI3K) is a regulatory enzyme with pleiotropic, essential functions that is a frequently altered driver of malignant progression. In particular, *PIK3CA* and *PIK3CB*, which encode catalytic isoforms of PI3K, are recurrently mutated and/or amplified in cancer, and *PTEN*, encoding a prominent negative regulator of the pathway, is frequently deleted^{12,13}. These alterations are prevalent in various tumor types, prompting extensive efforts to develop inhibitors of PI3K and its downstream effectors¹⁴⁻¹⁶. Unfortunately, these endeavors have proved challenging due to diffuse patterns of PI3K expression across non-malignant tissues and the dose-limiting toxicities that emerge secondary to their inhibition in these tissues¹⁷⁻¹⁹. Subsequent studies have pinpointed the presence of specific PI3K isoforms in distinct malignant tissue types, prompting the notion that modifying the function of a pivotal enzyme like PI3K might

95 be achievable in a tissue-selective manner. In light of this, advances have been made in the
96 development of inhibitors targeting the delta isoform of PI3K (encoded by *PIK3CD*), whose pattern
97 of tissue expression is notable for its abundance in lymphoid cells. Clinical trials with PIK3CD
98 inhibitors have demonstrated clinically-significant activity in patients with relapsed or refractory
99 CLL, although improvements to their specificity may be required to further optimize their toxicity
100 profile²⁰. This example underscores the promise of targeting the essential enzyme, PI3K, in a
101 tissue-specific manner based on isoform-dependency as a viable therapeutic strategy.

102 The specific isoform of PI3K, PIK3CG/p110 γ (also known as PI3K γ), was previously
103 described as a critical regulator of tumor immune evasion in myeloid cells, where it is the most
104 prominently expressed isoform among PI3K variants²¹⁻²³. In solid tumor studies, due to its immune
105 function, PIK3CG was also reported as a regulator of innate immunity during inflammation and
106 cancer. Consequently, PIK3CG inhibition using small-molecule inhibitors such as IPI-549 has
107 been used in combination with anti-PD-1 checkpoint inhibition to drive therapeutic antitumor
108 immunity^{21,24}. These findings have spurred the development of phase 1 clinical trials investigating
109 the antitumor activity of IPI-549 in combination with PD-1/PD-L1 inhibitors²⁵.

110 In this study, we establish that PIK3CG/p110 γ and its exclusive cognate regulatory
111 subunit, PIK3R5/p101, exhibit lineage-restricted expression and represent critical vulnerabilities
112 in AML, consistent with the findings of a recently published study²⁶. Further, we confirmed that
113 tissue-specific expression and dependency patterns of the PIK3CG/PIK3R5 heterodimer confer
114 isoform-specific control of downstream AKT signaling and, when lost, increase sensitivity to
115 venetoclax. Surprisingly, small molecules targeting PIK3CG recapitulate neither the proliferative
116 deficits nor the inhibitory signaling observed with genetic suppression of PIK3CG and PIK3R5.
117 This motivated the development of a PROteolysis TARgeting Chimera (PROTAC) degrader
118 molecule, which demonstrates efficacious PIK3CG degradation and markedly impairs AML cell
119 survival *in vitro* and in murine models.

RESULTS

PIK3CG and its Regulatory Subunit PIK3R5 Exhibit a Myeloid-Biased Expression Profile and Are Required for AML Cell Survival

To explore lineage-specific genetic dependencies in AML, we used publicly available primary patient data from The Cancer Genome Atlas (TCGA) and healthy donor tissue-derived data from the Genotype-Tissue Expression Project (GTEx) to compare gene expression in primary tumor and healthy samples across different tissue types. We observed upregulation of *PIK3CG* expression (encoding PIK3CG/p110 γ) in the myeloid compartment relative to other tissue types (**Figure 1A; Table S1**). This observation was confirmed by comparison of the GTEx data with the primary AML patient sample collection data from the BEAT-AML cohort²⁷ (**Figure S1A**). By contrast, *PIK3CA*, *PIK3CB*, and *PIK3CD*, encoding the PI3K isoforms PIK3CA/p110 α , PIK3CB/p110 β and PIK3CD/p110 δ , respectively, displayed widespread expression across many tissue types, confirming in agreement with previous studies, a specific role for PIK3CG in the myeloid compartment^{21,23} (**Figure 1A**). The restricted expression of *PIK3CG* is complemented by the expression of its exclusive, cognate regulatory subunit, *PIK3R5* (encoding PIK3R5/p101), which exhibits similarly restricted expression in myeloid normal tissues and upregulation in AML. Within the BEAT-AML cohort, *PIK3CG* and *PIK3R5* were significantly upregulated in patients who were subclassified in the French-American-British (FAB) monocytic 4 and 5 categories compared to those in other FAB subgroups (**Figure S1B**). No significant difference was observed in the expression of *PIK3CG* or *PIK3R5* among patients with *NPM1*-mutated AMLs, those carrying the t(8,21) and MLL-fusion alterations, or between patients at diagnosis and relapse after chemotherapy (**Figures S1C and S1D**). Only *PIK3R5* expression exhibited a significant increase in patients harboring the inv(16) alteration. A deeper correlative analysis between *PIK3CG* and *PIK3R5* expression and the leukemia cell state revealed that the expression level of these two genes is positively correlated with the expression of monocytic- and dendritic cell-like

transcriptomic features in AML cells²⁸, and negatively correlated with those related to the progenitor-like or the LSC17 gene signatures²⁹ (**Figures S1E and S1F**).

We then mined publicly-available ChIP-seq data to establish the binding pattern of the H3K27ac histone mark, which is associated with active transcription, at the promoter and gene body regions of *PIK3CG* and *PIK3R5* in primary samples from AML patients and cord-blood-derived CD34⁺ cells from healthy donors (**Figure 1B**). This analysis unveiled that several genomic regions in *PIK3CG* and *PIK3R5* were marked by H3K27ac in a significant proportion of AML patients and healthy donors. Notably, the increased signal of H3K27ac across the *PIK3R5* gene was more pronounced in the majority of AML patient-derived primary cells compared to normal CD34⁺ cells. This suggests heightened *PIK3R5* transcriptional activity in the malignant context, which is consistent with the substantial RNA upregulation of *PIK3R5* observed in AML relative to its healthy counterpart (**Figures 1A and 1B**).

To explore whether the increased expression of *PIK3CG* and *PIK3R5* in myeloid cells might be linked to a potential survival requirement in myeloid leukemias, we then examined the DepMap dataset to establish the dependency profile of the catalytic and regulatory subunits of PI3K across a wide range of cancer types. Of the four PI3K isoforms, *PIK3CG* was most essential in AML (and secondarily in ALL) with minimal essentiality in malignancies of non-hematopoietic origin (**Figure 1C**). By contrast, *PIK3CA* and *PIK3CB* were essential across malignancies of diverse tissue types. A selective dependency on *PIK3R5* was also observed in AML and Chronic Myelogenous Leukemia (CML), both related myeloid malignancies, while the regulatory subunits associated with *PIK3CA*, *PIK3CB*, and *PIK3CD* exhibited widespread essentiality across cancers of other tissues. All together, these data suggest that PIK3CG-PIK3R5 signaling may act as a lineage-restricted driver of disease progression, and a selective survival dependency in AML.

To validate the isoform-selective essentiality of PIK3CG in AML, we designed doxycycline (dox)-inducible short-hairpin RNAs (shRNAs) to knockdown *PIK3CA*, *PIK3CB*, *PIK3CD*, and

PIK3CG. AML cell viability was reduced following shRNA-mediated depletion of *PIK3CG* but not following suppression of the other catalytic members of the PI3K family, suggesting an isoform-specific role for *PIK3CG* in AML cell survival (**Figure 1D**). We then introduced a doxycycline-inducible CRISPR-Cas9 single-guide RNA (sgRNA) system targeting the catalytic subunit of *PIK3CG* in various AML cell lines. *PIK3CG* locus editing was confirmed using a TIDE assay³⁰ (**Figure S2A**). Knockout of *PIK3CG* resulted in a significant growth impairment of all AML cell lines tested, further evidencing a dependency on *PIK3CG* for the growth of AML cells in agreement with a recently published study²⁶ (**Figures 1E and 1F**). A similar CRISPR-Cas9 approach was then used to knockout the expression of *PIK3R5* and yielded a marked reduction in AML cell growth (**Figures 1G-1H, and S2A**). Using a colony formation assay, we further evidenced that both *PIK3CG* and *PIK3R5* gene suppression significantly dampened the colony-forming ability of multiple AML cell lines (**Figure 1I**). Of note, we observed a greater effect of sgRNA targeting *PIK3CG*/*PIK3R5* on colony forming capacity as compared to the viability assay. Finally, to interrogate whether *PIK3CG* knockout could affect AML progression *in vivo*, we assessed the bioluminescence of NOD-SCID gamma (NSG) mice injected with luciferase-expressing OCI-AML2 cells infected with either a non-targeting control (sgControl) or a *PIK3CG*-directed (sg*PIK3CG*) sgRNA. Mice transplanted with AML cells expressing sg*PIK3CG* demonstrated a significantly lower disease burden over time in comparison with animals injected with sgControl OCI-AML2 cells, indicating that AML cell dependency on *PIK3CG* signaling is conserved *in vivo* (**Figures 1J and S2B**).

***PIK3CG*/*PIK3R5* Repression Potentiates the Effect of Venetoclax in AML**

In order to evaluate whether the suppression of the *PIK3CG*-*PIK3R5* signaling axis could enhance AML sensitivity to candidate targeted therapies, we first correlated the expression of *PIK3CG* and *PIK3R5* with the response to 123 small-molecule inhibitors which were screened across primary AML samples as part of the BEAT-AML project²⁷ (**Figure 2A**). This effort led us to

191 identify that patients with high *PIK3CG* or *PIK3R5* expression exhibit a higher resistance to the
192 BCL2 inhibitor, venetoclax, which was recently approved by the FDA for the treatment of elderly
193 patients with AML. These results were reinforced by the fact that decreased venetoclax sensitivity
194 was predominantly found in patients classified in the FAB 4 and 5 subcategories, who also exhibit
195 higher levels of *PIK3CG* and *PIK3R5* expression (**Figures 2B and S1B**). Therefore, we
196 hypothesized that suppression of *PIK3CG* or *PIK3R5* may potentiate the anti-leukemic effect of
197 venetoclax.

198 We thus examined the effect of *PIK3CG* and *PIK3R5* knockouts on AML cell response to
199 venetoclax and to front-line chemotherapies routinely used in this disease, such as azacitidine,
200 cytarabine, daunorubicin. We also assessed the effect of these target knockdowns on AML cell
201 response to FLT3 and KIT inhibitors. Suppression of *PIK3CG* and *PIK3R5* consistently and
202 significantly decreased the area under curve (AUC) and half-maximal inhibitory concentration
203 (IC50) of venetoclax, but had no major effect on the other small-molecules tested, including the
204 FLT3 inhibitors gilteritinib and sorafenib, and the KIT inhibitors amuvanib and telatinib (**Figures**
205 **2C, S3A and S3B**). The potentiating effect of *PIK3CG* or *PIK3R5* loss on venetoclax sensitivity
206 was also validated in two additional AML cell lines, MOLM-14 and OCI-AML3 (**Figure 2D**).
207 Venetoclax combined with *PIK3CG* or *PIK3R5* targeting sgRNAs also reduced the colony-forming
208 capacity more than either perturbation alone in these AML cell lines (**Figure 2E**). In contrast, no
209 further sensitization of AML cells to venetoclax was observed upon knockout of the other PIK3
210 catalytic isoforms, *PIK3CA*, *CB*, and *CD* (**Figures 2F and 2G**).

211 To explore the importance of the PIK3CG-PIK3R5 signaling axis in AML progression and
212 sensitivity to venetoclax treatment in an *in vivo* system, we injected a pool of luciferase-expressing
213 GFP/Cas9-positive OCI-AML2 cells infected with either a non-targeting control or a *PIK3CG*-
214 directed sgRNA into NSG mice (**Figures 2H and 2I**). At the experimental endpoint (defined by
215 the control cohort time of death), we observed a profound decrease in the proportion of GFP-

positive leukemic cells in the bone marrow of mice transplanted with *PIK3CG* knockout cells along with a significant sensitization to venetoclax treatment, compared to mice treated with venetoclax alone (**Figure 2H**). Over time, disease burden was quantified through the measurement of a bioluminescence signal. Mice injected with *PIK3CG* knockout cells exhibited a lower overall disease burden compared to recipient animals injected with *PIK3CG* wild-type cells. This decreased disease burden was potentiated when mice were treated with venetoclax (**Figures 2I and S3C**). These results were corroborated by a significant increase in the overall survival of animals injected with *PIK3CG*-silenced AML cells or treated with venetoclax. Importantly, mouse survival advantage was further improved by the combination of *PIK3CG* knockout and venetoclax treatment (**Figure 2J**). Overall, these data suggest that specifically targeting the PIK3CG-PIK3R5 signaling axis can potentiate the effect of venetoclax both *in vitro* and *in vivo*.

AKT Signaling is Exquisitely Dependent on the PIK3CG/PIK3R5 Signaling Module in AML Cells

To characterize the PIK3CG-PIK3R5 signaling network, we performed tandem purification and mass spectrometry-based interactomic profiling of PIK3R5 in three different AML cell lines: MV4-11, OCI-AML2, and NOMO-1. We confidently identified 170 top-scoring PIK3R5 interactors based on a significant log₂ fold change of enrichment compared to the control (**Figure S4A**) and on identification only in PIK3R5 conditions with a significantly above average number of peptides (**Figure S4B**) in at least two out of the three cell lines profiled (**Figure S4C, Table S2**). Leveraging this comprehensive list of interactions, we constructed a STRINGdb-based physical interaction network (score > 0.5), categorized into distinct nodes which displayed pertinent sets of PIK3R5 interactors (**Figure 3A**).

A core node featured predominantly PIK3CG which consistently interacted with PIK3R5 across all profiled AML cell lines. This core complex was associated with critical kinase and transcription factor regulators of myeloid cells such as FLT3, RUNX1, and TET2, which are

commonly found mutated and dysregulated in myeloid neoplasia³¹. Notably, PIK3CG-PIK3R5 activity, predominantly controlled by G protein-coupled receptors (GPCRs), gathered various guanine nucleotide exchange-related factors (GEFs) to the PIK3CG/R5 core complex^{32,33}. This core complex was also physically associated with proteins linked to mitochondria and nucleopores, hinting at a biological link between PI3K gamma signaling, mitochondrial function, metabolism, and nucleocytoplasmic transport. Interestingly, the TORC2 complex comprising MTOR, RICTOR, and FKBP8, along with the R2TP/TEL chaperone complexes, were identified as significant interactors of PIK3CG/R5. These complexes were reported to regulate AKT activation levels. TORC2 directly phosphorylates AKT on Ser473 and facilitates Thr308 phosphorylation by PDK1, while R2TP/TEL2 stabilizes MTOR and modulates AKT through downstream regulation of AKT2 phosphorylation in the PI3K signaling pathway^{34,35}. Furthermore, activation of PIK3CG via GPCRs leads to the production of the versatile second messenger PtdIns(3,4,5)P3, serving as a docking site for pleckstrin homology domain-containing kinases, including AKT^{24,36}.

Based on these various observations, we sought to investigate whether the highly tissue-specific expression pattern of the PIK3CG-PIK3R5 signaling network in AML conferred isoform-specific control of downstream AKT signaling. We reasoned that if PIK3CG controls AKT signaling in AML cells, those cells should exhibit PIK3CG dependence proportional to their AKT dependence. We tested this in a panel of 15 AML cell lines and found that *PIK3CG* dependency was correlated with dependency on *AKT1* and *AKT2* in AML cell lines but not in cell lines from other tissues (**Figures 3B and S5A**). Given the correlation between *PIK3CG* dependency and *AKT1/2*, we used a CRISPR/Cas9 drug-modifier screen to identify a common set of genes that significantly altered sensitivity to MK-2206, a pan-AKT inhibitor. Cells harboring sgRNAs targeting *BCL2* were most depleted in MK-2206 modifier screens, while cells harboring sgRNAs targeting negative regulators of TOR signaling (*TSC1*, *TSC2*, *NPRL2*) were enriched (**Figure 3C**). These

findings are consistent with our data and others', positioning the venetoclax target, BCL2, and MTOR as protein candidates whose inhibition synergistically enhances the effects of PI3K pathway inhibition^{37,38}. In this cellular context, the potentiation of AKT inhibition appears to be selective to *BCL2* suppression, as no other anti-apoptotic BCL2-family proteins scored as sensitizers like BCL2. Furthermore, topoisomerase-encoding genes, which are targets of anthracyclines such as daunorubicin, and polymerase-encoding genes affected by cytarabine, did not score as noticeable sensitizers to MK-2206 (**Figure S5B**). Collectively, these data nominated AKT as a potential downstream signaling pathway that might be selectively activated by PIK3CG-PIK3R5, possibly accounting for the increased sensitivity of AML cells to venetoclax.

To further confirm the connection between PIK3CG-PIK3R5 with AKT signaling, we sought to evaluate the consequence of CRISPR-Cas9-mediated *PIK3CG* knockout on AKT signaling. We showed by western blot that *PIK3CG* and *PIK3R5* knockouts in OCI-AML3 and OCI-AML2 cells diminish the phosphorylation of AKT and its previously reported downstream substrates, PRAS40 and TSC2 (**Figure 3D**). The phosphorylation levels of both AKT1 and AKT2 isoforms were decreased upon suppression of *PIK3CG* and *PIK3R5* (**Figure 3E**). Whereas the silencing of *PIK3CG* did not noticeably affect the expression levels of BCL2, and the pro-apoptotic proteins BAX, PUMA, and BIM, we observed a decrease in MCL1 (**Figure 3F**).

To determine whether AKT signaling relies selectively on PIK3CG in AML cells, we employed doxycycline-inducible shRNAs to knock down the expression of *PIK3CA*, *PIK3CB*, and *PIK3CD*, and revealed that *PIK3CG* suppression yielded predominantly a decrease in the activation of AKT, affecting both T308 and S473 phosphorylation sites, in contrast to the other PIK3 catalytic isoforms (**Figure 3G**). A similar approach employed to selectively reduce the expression of the PI3K regulatory subunits enabled us to confirm that only shRNAs directed against *PIK3R5* significantly dampened AKT phosphorylation compared to the inhibition of the other regulatory subunits (**Figures 3H and 3I**). Conversely, overexpression of wild-type *PIK3CG*

under a constitutive EF1 α promoter resulted in hyperactivation of AKT signaling. We then introduced an shRNA directed against the 3' UTR region of *PIK3CG* which was capable of knocking down endogenous *PIK3CG* without affecting exogenously expressed *PIK3CG* cDNA lacking the 3' UTR. Expression of wild-type *PIK3CG* cDNA was able to fully rescue AKT suppression secondary to the suppression of endogenous *PIK3CG* (**Figure 3J**). These data indicate that PIK3CG is both necessary and sufficient for the activation of AKT signaling in AML.

We finally sought to investigate whether the modulation of GPCR functions could affect PIK3CG-mediated AKT activation. CXCL12 (also known as SDF1 α) is the ligand for CXCR4, a GPCR that signals to downstream pathways including the PI3K/AKT pathway. The CXCL12/CXCR4 signaling axis has been implicated in maintenance of the leukemic niche³⁹, and both the receptor and ligand are upregulated in AML cells relative to normal hematopoietic cells (**Figures 3K and S5C**). Pertussis toxin targets G-proteins and broadly impairs the ability of GPCRs to activate PI3K/AKT and other signaling pathways⁴⁰. The addition of pertussis toxin to AML cell lines reduced phosphorylation of AKT, demonstrating the predominant role of GPCRs over other ligand-binding receptors across AML cell lines to modulate downstream AKT signaling (**Figure 3L**). Because PIK3CG-PIK3R5 is activated via GPCRs, whereas other isoforms are predominantly under the control of receptor tyrosine kinases (RTKs)⁴¹, we interrogated the effect of *PIK3CG* suppression in the presence or absence of the CXCR4 GPCR-activating ligand, CXCL12 (**Figure 3M**). We determined that, following *PIK3CG* knockout, CXCL12 failed to activate downstream AKT signaling. These data provide evidence that PIK3CG mediates AML cell AKT signaling downstream of GPCRs, including CXCR4.

Small-Molecule Inhibitors of PIK3CG Do Not Sustain Long-Term AKT Inactivation and AML Cell Growth Impairment

Given the dependency we observed on *PIK3CG* in several AML models, we anticipated that small-molecule inhibitors targeting PIK3CG would efficiently alter AML cell growth.

Surprisingly, however, the pharmacological inhibition of PIK3CG using IPI-549 and AZ2, two PIK3CG-isoform selective small molecule inhibitors, did not result in a marked reduction in AML cell viability and colony-forming capacity when compared to the genetic ablation of PIK3CG and PIK3R5 using *PIK3CG*- and *PIK3R5*-directed sgRNAs (**Figures 4A and 4B**). Of note, no further reduction in cell growth was measured with the addition of fresh IPI-549 or AZ2 every 24 hours, suggesting that the blunted activity of these small molecules relative to *PIK3CG/PIK3R5* knockout was not caused by drug instability (**Figure 4C**). We therefore postulated that these small-molecule inhibitors might not durably inhibit PIK3CG-mediated AKT signaling. We substantiated our hypothesis by showing that the long-term suppression of AKT phosphorylation was more effective when using sgRNAs targeting *PIK3CG* or *PIK3R5* compared to treatment with IPI-549 and AZ2 (**Figure 4D**). While AKT phosphorylation decreased one hour after treatment with IPI549 and AZ2, we observed reactivation of AKT at 72 hours post-treatment. Remarkably, this activation persisted despite retreatment of the cells with fresh drugs for one hour (**Figure 4E**). In contrast, the AKT inhibitor MK-2206, used here as a positive control for AKT signaling inhibition, repressed AKT phosphorylation durably (**Figures 4D and 4E**). Taken as whole, these findings imply that existing small molecule inhibitors of PIK3CG are inadequate to achieve a durable reduction in downstream AKT signaling, and consequently, they do not attain the same level of cytotoxicity as *PIK3CG* and *PIK3R5* knockout. Conversely, the genetic suppression of *PIK3CG* and *PIK3R5* effectively prevents pathway reactivation, leading to a sustained and effective blockade of AKT phosphorylation. Therefore, a novel therapeutic approach for targeting PIK3CG, one that ensures a sustained disruption of PIK3CG/PIK3R5-mediated AKT signaling in AML cells, was needed.

As an alternative strategy for pharmacologically targeting PIK3CG, we opted to harness recent advancements in targeted protein degradation. We employed a PROteolysis TARgeting Chimera (PROTAC) system, in which AZ2, a PIK3CG-isoform selective inhibitor, was conjugated to a CEREBLON-targeting moiety. We capitalized upon the presence of an acetyl moiety on the

337 AZ2 parental compound that is orientated towards the outside of the kinase pocket to attach a
338 linker and a subsequent CEREBLON-recruiting moiety (**Figure 4F**). We discovered a lead
339 compound, designated as ARM165, which was synthesized from AZ2 through a 5-step chemical
340 pathway (**Figure S6**). To confirm that ARM165 targets PIK3CG, we treated OCI-AML2 cells with
341 increasing doses of ARM165 and assessed PIK3CG protein levels through western blot analysis.
342 Within 24 hours, we achieved 50% degradation of PIK3CG, but not PIK3R5, at a concentration of
343 1 μ M ARM165 (**Figures 4G**). We did not notice any major hook effect up to 10 μ M ARM165. The
344 absence of hook effect was already reported by other groups using other PROTAC-based
345 molecules. It was attributed to a favorable protein/protein interaction that broadens the
346 concentration range in which ternary complex formation prevails over binary complexes⁴²⁻⁴⁵.
347 Therefore, we may be in a scenario where PIK3CG and CRBN bind cooperatively in the presence
348 of ARM165. Co-treatment of cells with the proteasome inhibitor bortezomib fully rescued the loss
349 of PIK3CG protein induced by ARM165, suggesting that ARM165 reduces PIK3CG levels through
350 proteasome-mediated degradation. Additionally, co-treatment of cells with ARM165 and
351 lenalidomide, which binds to the same site on CEREBLON, competed with ARM165 to block
352 PIK3CG degradation (**Figure 4H**). Consistent with the proteasome-induced degradation of
353 PIK3CG by ARM165, a lysine to arginine mutant form of PIK3CG in which lysine residues between
354 position 427 and 597 were mutated into arginine, was resistant from the effect of ARM165 (**Figure**
355 **4I**). Ultimately, we confirmed that ARM165 significantly diminished the colony-forming capacity of
356 OCI-AML2 cells through a selective degradation of PIK3CG because cells lacking *PIK3CG*, or
357 *CRBN* (encoding CEREBLON), were resistant to the PROTAC degrader (**Figures 4J and 4K**).
358 Through an unbiased proteomic-based analysis conducted on HEK293T cells expressing
359 exogenous PIK3CG, we confirmed that PIK3CG is the most significant ARM165 target (**Figure**
360 **4L, Table S3**).

To determine if ARM165 could effectively inhibit downstream AKT signaling to a similar extent as sgRNAs targeting *PIK3CG* and *PIK3R5*, we compared the level of AKT phosphorylation in OCI-AML2 cells infected with CRISPR-Cas9 sgRNAs targeting *PIK3CG* and *PIK3R5* or treated with 1 μ M ARM165. Cells treated with ARM165 demonstrated a reduction in PIK3CG comparable to that achieved by CRISPR-Cas9 targeting sgRNAs, resulting in a similar level of disruption in downstream AKT signaling (**Figure 4M**). Importantly, ectopic expression of a constitutively activated, myristoylated form of AKT alleviated markedly the ARM165-induced decreased AML cell growth (**Figure 4N**). Collectively, these findings support ARM165 as a newly developed selective heterobifunctional degrader of PIK3CG which durably alters AKT signaling in AML cells.

Degradation of PIK3CG Demonstrated Superior Cytotoxic Performance Relative to Existing Small-Molecule Inhibitors of PIK3CG

We then questioned how the PROTAC-mediated degradation of PIK3CG and the subsequent disruption of AKT signaling could affect the viability of AML cells. To investigate this, we compared the impact of both ARM165 and the parental AZ2 with that of an analogous molecule, ARM204, featuring a single R group alteration—replacing the hydrogen atom of the imide function with a methyl group (**Figure S7B**). This minor structural modification rendered the compound incapable of binding to CRBN⁴⁶. Increasing concentrations of ARM165 significantly affected the growth of these cell lines, whereas AZ2 and ARM204 had minimal anti-leukemia effects (**Figures 5A, 5B, and S7A**). Because the dependency on PIK3CG and its regulatory subunit PIK3R5 was primarily observed in myeloid cells, we hypothesized that the degrader's efficacy would be more specific to this cell type. Consequently, we assessed the ARM165 degrader's effect on a range of non-AML cell lines. Our results demonstrated unambiguously that these cell lines were mostly insensitive to ARM165 (**Figure 5B**). These data support the notion that ARM165 could be used as a lineage-specific treatment in AML to avoid the dose-limiting effects of targeting PI3K in non-hematopoietic tissues. To expand the applicability of our results

to a wider range of AML cell models, we exposed primary cells isolated from AML patients to AZ2 and ARM165 (**Table S4**). ARM165 significantly compromised the viability of primary cells when compared to its parental compound, AZ2, thereby confirming the enhanced potency of the PIK3CG degrader in affecting AML cell growth (**Figure 5C**).

To further assess ARM165 activity, RNA-sequencing data from OCI-AML2 and MOLM-14 cells treated with vehicle, AZ2, or ARM165 were projected onto a principal component analysis (PCA) plot to convey the most variation in the dataset. This confirmed that ARM165-treated cells displayed a markedly altered transcriptional profile compared to those treated with the parental compound AZ2, which showed minimal change relative to untreated cells (**Figure 5D**). An open-ended overrepresentation analysis identified P53- and apoptosis-related gene sets as being significantly activated by ARM165, with cut-offs at p-values of ≤ 0.05 and false discovery rates (FDR) of ≤ 0.25 . Conversely, oxidative phosphorylation-, cell cycle-, and AKT/MTOR-related gene sets were significantly repressed (**Figure 5E**). The expression levels of leading-edge genes from each of these representative biological pathways were indeed reliably dysregulated by ARM165, but not by AZ2 (**Figure 5F**). The increased proportion of Annexin V-positive MOLM-14 and OCI-AML2 cells in response to ARM165 confirmed that this PROTAC degrader promotes apoptosis in AML cells (**Figure 5G**). Finally, to determine the relative selectivity of ARM165 towards PIK3CG using these transcriptomic data, we hypothesized that patients with the highest expression of *PIK3CG* would be more likely to respond to ARM165 treatment. Employing single-sample Gene Set Enrichment Analysis (ssGSEA), we therefore queried the predicted response of patients to ARM165 based on their *PIK3CG* expression. As anticipated, patients with elevated levels of *PIK3CG* were significantly more likely to respond to ARM165 treatment, further demonstrating ARM165's favorable selectivity towards PIK3CG (**Figure 5H, Table S5**).

PIK3CG Degradation Potentiates the Effect of Venetoclax across Multiple AML Models

Considering the potentiation effect that we previously observed with sgRNAs targeting *PIK3CG* and venetoclax, we investigated whether the ARM165 degrader would sensitize AML cells to venetoclax treatment to a similar extent. We determined that increasing doses of ARM165 significantly amplified the effect of venetoclax on reducing the growth and colony-forming capacity of various AML cell lines, in contrast to cells treated with the parental AZ2 compound (**Figures 6A, 6B, and S8A**). ARM165 sensitized cells to venetoclax to a greater extent than to daunorubicin and cytarabine, for which ARM165 only mildly enhanced the anti-leukemia effect (**Figure S8B**). In addition, in OCI-AML2 cells, ARM165 maximized only the cell growth defect induced by venetoclax, not by MCL1 or BCL-X_L inhibition using S63845 (MCL1 inhibitor), WEHI-539 (BCL-X_L inhibitor), or A-1331852 (BCL-X_L inhibitor), despite the basal sensitivity of these cells to MCL1 inhibition (**Figure 6C**). Although the sensitivity to venetoclax may vary among different AML cell types, these results suggest that *PIK3CG* degradation is more likely to enhance the efficacy of venetoclax. This potentiation of venetoclax's effect was also shown in primary patient cells. ARM165 alone induced a marked decrease in colony formation when compared to parental AZ2, and this effect was further enhanced when combined with venetoclax (**Figure 6D**). We finally evaluated the synergistic activity of ARM165 and venetoclax using an excess over Bliss analysis over a wide range of concentrations. The analysis pointed out that ARM165 and venetoclax act synergistically to impair AML cell viability (**Figure 6E**). Notably, this synergistic activity of ARM165 with venetoclax was significantly greater than that of AZ2 with venetoclax across nine primary patient samples (**Figure 6F**).

In light of reports that durable response to therapy in AML necessitates an abrogation of leukemia-initiating cells (LICs), we investigated the impact of ARM165 on the LIC fraction of a *Cbfb-MYH11*-driven mouse model of AML. *Cbfb-MYH11*-positive cells were treated *ex vivo* with either ARM165 or AZ2 prior to reinjection into sublethally-irradiated secondary recipient mice at various cell concentrations. Using extreme limiting dilution analysis, we observed a 4.9-fold

decrease in LIC frequency in secondary recipients injected with blasts treated with ARM165 compared to those engrafted with blasts exposed to AZ2 (**Figure 6G**). These promising results led us to evaluate the impact of ARM165 on mice injected with *Cbfb-MYH11*-driven leukemic cells. The large molecular weight of PROTACs and other heterobifunctional molecules is well-known for presenting challenges in terms of solubility and bioavailability for *in vivo* testing. Nevertheless, we initially evaluated both intraperitoneal (IP) and intravenous (IV) routes of administration for ARM165. We established that IV administration of ARM165 over four consecutive days was the most promising treatment regimen as it slowed down disease progression when compared to IP injection. IP administration of ARM165 was ineffective in affecting leukemic cell progression due to the rapid precipitation of ARM165 in the peritoneal cavity of the animals (not shown). Employing the IV treatment regimen in mice injected with *Cbfb-MYH11*-driven AML cells resulted in a significant reduction in leukemia burden in bone marrow when compared to animals treated with either vehicle or AZ2 (**Figure 6H**). The assessment of leukemic burden of the spleen as a secondary site of leukemic infiltration confirmed the anti-leukemia effect of ARM165, mirroring the results observed in the bone marrow (**Figure 6I**). This treatment regimen did not significantly alter the weight of naive mice (**Figure S9A**). It induced a slight yet significant decrease in the hematopoietic stem and myeloid progenitor cell fraction in the bone marrow and spleen monocytes, and an increase in blood hematocrit and hemoglobin levels (**Figure S9B**).

Finally, we investigated the anti-leukemic effect of ARM165 in combination with venetoclax in i) syngeneic mice transplanted with *Cbfb-MYH11*-driven leukemic cells and ii) NSG-S mice xenografted with AML primary patient cell material. In both mouse models, animals treated with the combination of these two drugs displayed a significantly reduced leukemic burden compared to those treated with ARM165 or venetoclax alone (**Figure 6J**). These findings confirm the promise of PROTAC-based PIK3CG destabilization, whether used alone or in combination with

venetoclax, as a therapeutic approach with potential advantages over existing PIK3CG-targeting small-molecule inhibitors.

DISCUSSION

The success of targeted therapies in cancer is intricately linked to the capacity to identify molecular subtypes within tumors and discern the critical dependencies responsible for their onset and progression. In this context, the concept of lineage addiction emerged as the idea that certain cancer types are reliant on the abnormal activation of genes or pathways that are generally essential for the development and function of their lineage of origin. The discovery that the master transcription factor regulator of melanocyte function, MITF, acts as a melanoma oncogene constitutes an informative example in this regard⁴⁷. Melanoma, originating from melanocytes, often retains its reliance on MITF. Consequently, MITF serves as a lineage-specific controller, functioning within normal cells and being similarly employed by melanoma cells for progression and propagation. Consistent with this, several melanoma cell lines exhibit increased dosage at a region of chromosome 3p containing *MITF* and the genetic depletion of this lineage addiction has proven to be especially effective in melanoma⁴⁷. In our study, we confirmed that, similar to the exquisite function of MITF in melanocytes, the expression of *PIK3CG* and its regulatory subunit, *PIK3R5*, is predominantly restricted to the myeloid compartment, thereby completing previous observation that *PIK3CG* is highly expressed in myeloid cells²¹⁻²³. Using a variety of genetic tools, we showed that the suppression of these genes has a significant impact on AKT signaling and the growth of AML cells, an effect which was, in contrast, not markedly observed upon knockdown of other PI3K isoforms. Despite the expression of other PI3K isoforms in AML cells, our findings, and those of a corroborating study published during the review of this manuscript²⁶, suggest that *PIK3CG* and *PIK3R5* constitute AML-specific vulnerabilities, primarily because of their prominent role in regulating AKT signaling in comparison to the other PI3K isoforms. Targeting this 'lineage-specific signaling addiction' may enable therapy to be directed toward the tissue compartment

where malignancy is present, creating the potential for a therapeutic window that can spare non-malignant tissues.

We demonstrated that targeting PIK3CG can enhance the effectiveness of the BCL2 inhibitor venetoclax, which is a newly approved standard-of-care therapy for elderly patients with AML⁴⁸. This increased sensitivity to venetoclax is likely a direct result of AKT inhibition. We established this through a whole-genome CRISPR screen, which ranked BCL2 as one of the top sensitizers to the AKT inhibitor MK-2206. The underlying mechanism of this interrelationship between AKT and BCL2 may lie in the regulation of the anti-apoptotic protein MCL1. Inhibition of AKT and mTOR signaling has been shown to decrease MCL1 protein levels in AML cells⁴⁹, and in multiple cancer models, MCL1 expression has been found to be anti-correlated with the response to venetoclax⁵⁰. The decreased expression of MCL1 upon PIK3CG and PIK3R5 signaling inhibition may thus play a substantial role in potentiating the effect of venetoclax, though additional studies are required to fully elucidate the mechanism underlying venetoclax sensitization.

The small-molecule inhibitor IPI-549 was developed to target the mechanism of immune suppression in tumorigenesis^{21,24,51}, and subsequently, other PIK3CG-targeting compounds including AZ2 were developed⁵². Despite these developments, IPI-549 remains the only PIK3CG-targeting molecule under clinical investigation to date²⁵. Considering the evidence that merely inhibiting PIK3CG-mediated AKT activation with these small-molecule kinase inhibitors was unable to achieve a durable elimination of AML cells, we developed a comprehensive targeting strategy using a CRBN-based PROTAC system to degrade PIK3CG. This approach demonstrated a significant anti-leukemia effect. Notably, several studies speak to the dual scaffolding and catalytic role of PIK3CG in promoting downstream signaling events. A comparison of knockout versus kinase-dead knock-in mice yielded critical insights into the non-catalytic functions of PIK3CG⁵³. Specifically, the contrasting phenotypes between *PIK3CG*-deficient

versus *PIK3CG* kinase-dead mice revealed that this enzyme serves as a molecular scaffold orchestrating cellular signaling complexes independently of its lipid kinase activity^{54,55}. For instance, it has been reported that *PIK3CG* binds to and regulates the activity of phosphodiesterase 3B (PDE3B) independently of its catalytic activity, likely as part of a protein complex⁵⁶. The disruption of PDE3B activity in *PIK3CG* knockout mice leads to increased cAMP levels, a phenomenon seen exclusively in *PIK3CG*-knockout mice, not in *PIK3CG* kinase-dead animals. These scaffolding functions are notably selective, and the absence of a specific PI3K isoform is unlikely to be compensated for by others. Interestingly, these functions have been well-documented for GPCR-dependent PI3-kinases like *PIK3CG*, and they may act in concert or independently from the kinase activity. For example, *PIK3CG*'s kinase-independent scaffold functions are intertwined with its kinase activity in diet-induced obesity, while *PIK3CG* plays a role in insulin signaling independently of its kinase activity^{55,57-59}.

The findings that PI3K isoform scaffolding and kinase activity functions can be disentangled to affect a broad array of cellular functions highlights how various PROTAC-based degradation approaches, similar to the one we have carried out for targeting *PIK3CG*, can result in more profound downstream signaling alteration and significant variations in functional outcomes compared to the targeting of kinase function alone. This extends the potential application of this technology for more effective PI3K signaling inhibition, with possible implications for clinical use. Similar to our findings with *PIK3CG* degradation, targeted protein degradation can often outperform small molecule inhibitors initially designed for the same protein target. For example, dBET1 exhibited a greater apoptotic response in primary AML cells compared to its precursor, JQ1, emphasizing the potential superiority of BET degradation over bromodomain inhibition⁶⁰. Additionally, PROTAC degraders targeting STAT3 and STAT5 have demonstrated significantly greater potency than small molecule inhibitors, which were reported to lack adequate potency and selectivity^{61,62}. Similarly, the development of a selective FAK kinase

533 degrader exhibited improved activity in downstream signaling, cancer cell viability, and migration
534 compared to FAK kinase inhibitors⁶³.

535 The results presented here argue for cancer therapeutics specifically designed to target
536 dependencies driven by proteins with tissue- and/or tumor-restricted expression. Our data also
537 provide a proof-of-concept that the degradation, rather than inhibition, of signaling molecules,
538 such as PIK3CG, could offer improved therapeutic benefits for patients, and more sustained
539 response to adjuvant therapy regimens. Further efforts are necessary to enhance the solubility
540 and *in vivo* bioavailability of our degrader, thereby creating a pharmacologically more efficient
541 preclinical-grade version which could open the path for promising clinical development.

METHODS

Cell Culture and Reagents

Cell lines were either purchased from the American Type Culture Collection (ATCC) or the Duke University Cell Culture Facility (CCF), and MOLM-14 cells were provided by Dr. Scott Armstrong (Dana-Farber Cancer Institute, Boston, Massachusetts). Identity of all cell lines was confirmed by short tandem repeat loci profiling. All cell lines were tested negative for Mycoplasma using MycoAlert PLUS Mycoplasma Detection Kit (Lonza #LT07-705). All cell lines were maintained in RPMI 1640 (Sigma #R2405) supplemented with 1% penicillin–streptomycin and 10% FBS (Sigma # F2442) in a humidified incubator at 37°C with 5% CO₂. HEK293T cells were maintained in DMEM (Sigma #D6429) supplemented with 10% FBS and 100U/mL penicillin–streptomycin (Sigma #P4333). Cells infected with shRNA and sgRNA constructs were maintained in culture with 1µg/ml Puromycin and 1µg/ml Doxycycline three days prior to fluorescence activated cell sorting and thereafter. Venetoclax (HY-15531), IPI-549 (HY-100716), MK-2206 (HY-10358), AZ2 (HY-111570), S63845 (HY-100741), WEHI-539 hydrochloride (HY-15607A), A-1331852 (HY-19741), Quizartinib (HY-13001), Sorafenib (HY-10201) and Gilteritinib (HY-12432) were purchased from MedChemExpress. Telatinib (S2231) and Amunatinib (S1244) were purchased from SelleckChem.

Patient Profiling and Primary Patient Sample Preparation

Patient samples were collected from AML patients, from whom informed consent had been given (including for sex collection) as part of an ongoing clinical registry at St Louis Hospital (THEMA, IRB approval #IDRCB2021-A00940-41). Samples were anonymized and stored at the St Louis Hospital Tumor biobank, as declared to the ministry of Higher Education, Research and Innovation. The use of these primary patient cells for experimental procedures derived from clinical practice was approved by the INSERM IRB. In accordance with the declaration of Helsinki

and French protection of personal data law, only anonymized clinical data were made available to research teams. Sex of patients has been collected on medical charts and is reported in **Table S4**. No race, ethnicity, or socially relevant data is reported in this study. Cytogenetic analyses required karyotyping and fluorescence *in situ* hybridization studies guided by karyotype. Genetic profiling consisted of fragment analysis for *NPM1*, *FLT3* and *IDH1/2* mutational status.

Mononuclear cells from patients with AML were isolated using Ficoll-Paque PLUS (GE Healthcare #17-1440-02) and red blood cells were lysed (Sigma # R7757). For methylcellulose and synergy assays, cells were maintained in RPMI 1640 medium supplemented with 20% FBS, 20ng/mL IL3 (PeproTech, #200-03), 20ng/mL IL6 (PeproTech, #200-06), 20ng/mL GM-CSF (PeproTech, #300-03), 10ng/mL G-CSF (PeproTech, #300-23), 10ng/mL EPO (PeproTech, #100-64), 50ng/mL TPO (PeproTech, #300-18), 100ng/mL FLT3-Ligand (PeproTech, #300-19), and 100ng/mL SCF (PeproTech, #300-07).

AML patients H3K27ac ChIP-seq Analysis

H3K SRA database was accessible under accession number SRP103200. Sequencing reads were aligned to the human hg19 version of the genome using Bowtie2⁶⁴ and duplicate reads were marked using Picard tools MarkDuplicates. Normalized bigwig files for gene track representations were generated using Deeptools⁶⁵ with the --normalizeUsing RPKM --extendReads 200 --smoothLength 150 --ignoreDuplicates options. Normalized density signals from *PIK3CG* and *PIK3R5* gene were extracted using bwtool⁶⁶ and density heatmaps with average signal bar plots were generated in R using iheatmapr package.

In vitro Drug Sensitivity Assays

Cells were seeded in 384-well plates, with between 5 and 7 replicates (Corning, #3570). A range of 10 descending concentrations plus a control vehicle-treated well were plated per drug tested. ATP content was measured using CellTiter-Glo® (Promega, #G7573) per manufacturer's

instructions. Relative cell viability was determined by normalizing raw luminescence values to either DMSO or the indicated background drug. IC50 and AUC values were approximated from dose-response curves plotted using the GraphPad/Prism 8 software.

***In vitro* Synergy Assays**

Cells were seeded in 384-well plates, with 4 replicates per concentration combination of venetoclax, and AZ2 or ARM165. Drugs were diluted 1:2 across, with 10 descending concentrations of venetoclax and 7 descending concentrations of ARM165. Maximum applied concentration of venetoclax and ARM165 were 5 μ M and 5 μ M, respectively. Synergy matrix was determined using Bliss additive synergy analysis using the following formula: $C=A+B-A*B$. (A= effect of agent 1. B= effect of agent 2. C= an expected effect of the combined response).

Plasmids and sgRNA Constructs

sgRNA constructs directed against human and murine PIK3CG, PIK3R5, PIK3CA, PIK3CB and PIK3CD (sequences listed below) were cloned into TCLV2 vector (addgene #87360). 5 μ g of TCLV2 backbone plasmid was digested and dephosphorylated in 60 μ l reaction containing 1X Fast digest Buffer (Fermentas), Fast digested BsmBI (Fermentas) and 1mM DTT, FastAP (Fermentas) for 30 min at 37 °C. Plasmids were gel purified using QIAquick Gel Extraction Kit. 100 μ M of sense and antisense of sgRNA oligo were phosphorylated and hybridized in a 10 μ l reaction containing 1X T4 ligation buffer and T4 PNK (NEB M0201S) at 37°C for 10 minutes; 95 °C for 5 minutes and then ramped down from 25 °C to 5 °C/min. The phosphorylated and digested BsmBI sgRNA were ligated into BsmBI digested TCLV2 plasmid in a 10 μ l reaction containing 1X Quick ligase buffer (NEB), diluted oligo duplex and Quick ligase (NEB M2200S) for 10 minutes at room temperature. For the inducible ectopic expression of PIK3R5, a codon-optimized 3xFlag-HA-*PIK3R5*-encoding gBlock (IDT) was PCR-amplified, digested using NheI and AgeI enzymes prior to its cloning into a neomycin-selectable doxycycline-inducible pCW57-Crimson vector. This

vector enabled flow cytometry-based sorting of cells overexpressing 3xFlag-HA-PIK3R5 using the Crimson fluorescence marker. For the overexpression of AKT, cells were infected with the lentiviral plasmid carrying Myristoylated AKT (addgene #64606) or the control (addgene #64648) as previously described⁶⁷. PIK3CG lysine into arginine mutants was generated by synthesizing a gBlock fragment in which lysines at position 437, 444, 455, 457, 490, 510, 531, 553, 572, 584, 587, and 597 were converted into arginines. This gBlock was subsequently cloned in a pLVX-puromycin vector.

Designation	Species	Target Sequence
sgPIK3CG_1	Homo Sapiens	GAAGGCTTGGGACTCCTCGG
sgPIK3CG_2	Homo Sapiens	TGGACTGAAAGCAGGAGCGC
sgPIK3R5_1	Homo Sapiens	GATCCTGCAGAAGACCCGAG
sgPIK3R5_2	Homo Sapiens	GCTGCCTCAGTGCTTACCTG
sgPi3kcg_1	Mus Musculus	GGTACCAGGAGTATCATCTG
sgPi3kcg_2	Mus Musculus	GTACGTGTCGCTGTACCACG
sgCRBN_1	Homo Sapiens	TATGTTTTTATATAGTACCT
sgCRBN_2	Homo Sapiens	ATGGTGGCAGAAATACCAGA
sgPIK3CA	Homo Sapiens	TTATTAATGTAGCCTCACGG
sgPIK3CB	Homo Sapiens	TGTAGCGTGGGTAAATACGA
sgPIK3CD	Homo Sapiens	GATGTGCCAATTCTGCGAGG

Western Immunoblotting

Western immunoblotting was performed as previously described⁶⁸ using cell lysates normalized for total protein content; cells were resuspended in lysis buffer (Cell Signaling Technologies, #9803S) supplemented with Halt protease and Phosphatase Inhibitor cocktail, EDTA-free (Thermo Fisher Scientific, #78443). Membranes were probed with primary antibodies overnight (16 hours):

Target	Provider	Reference
ACTIN	Fisher Scientific	11314533

P-AKT (T308)	CST	4056
P-AKT (S473)	CST	4060
AKT	CST	4691
PIK3CG / p110 γ	Provided by Prof. Matthias P. Wymann	
PIK3R5 / p101	CST	5569
P-PRAS40 (T246)	CST	2997
PRAS40	CST	2610
P-TSC2 (T1462)	CST	3617
TSC2	CST	4308
PIK3CA / p110 α	CST	4249
PIK3CB / p110 β	CST	3011
PIK3CD / p110 δ	CST	34050
PIK3R1 / p85	CST	4292
P-AKT1 (S473)	CST	9018
p-AKT2 (S474)	CST	8599
T-AKT1	CST	2938
T-AKT2	CST	3063
BCL2	CST	4223
MCL1	CST	5453
PUMA	CST	98672
BIM	CST	2933
BAX	CST	5023

627

628 **CXCL12 Cytokine Experiment**

629 Cells were incubated in serum free RPMI-1640 medium for one hour prior to spiking with
630 200ng/ml CXCL12/SDF-1a (PeproTech, #300-28A). After 30 minutes, cells were harvested,
631 washed twice, and pellets produced for western blotting.

632 **Generation of Stably-Expressing Doxycycline-Inducible shRNA Cell Lines**

633 Inducible expression of shRNAs was achieved as previously described using a
634 doxycycline-inducible pLKO-Tet-On lentiviral system⁶⁹. Lentivirus was produced and cells were
635 transduced as previously described⁶⁸. Following selection with puromycin, shRNA-transduced
636 cells were treated with doxycycline (75ng/mL) for 72 hours prior to analysis or experimentation.

637 shPIK3CA: CCGGAATGAAAGCTCACTCTGGATTCTCGAGAATCCAGAGTGAGCTTTTCATTTTTTTG

638 shPIK3CB: CCGGGCGGGAGAGTAGAATATGTTTCTCGAGAAACATATTCTACTCTCCCGCTTTTTTG

639 shPIK3CD: CCGGGACCCAGAAGTGAACGACTTTCTCGAGAAAGTCGTTCACTTCTGGGTCTTTTTTG

640 shPIK3CG_1: CCGGGCAGAGCTTCTTCACCAAGATCTCGAGATCTTGGTGAAGAAGCTCTGCTTTTTG
641 shPIK3CG_2: CCGGGCCCTATCAAATGAAACAATTCTCGAGAATTGTTTCATTTGATAGGGCTTTTTG
642 shPIK3CG 3'UTR: CCGGGCCTTATCCATTTCCCATTTACTCGAGTAAATGGGAAATGGATAAGGCTTTTTTG
643 shPIK3R1: CCGGCCTTCAGTTCTGTGGTTGAATCTCGAGATTCAACCACAGAACTGAAGGTTTTTG
644 shPIK3R2: CCGGGCAGATGAAGCGTACTGCAATCTCGAGATTGCAGTACGCTTCATCTGCTTTTTG
645 shPIK3R3: CCGGGCTTTGGACAACCGAGAAATACTCGAGTATTTCTCGGTTGTCCAAAGCTTTTTG
646 shPIK3R5: CCGGCAGGATCTATAAACTCTTCAACTCGAGTTGAAGAGTTTATAGATCCTGTTTTTG
647 shPIK3R6: CCGGCCAGATCTACACAGTCAAGATCTCGAGATCTTGACTGTGTAGATCTGGTTTTTG

648 **RT-qPCR**

649 RNA was isolated from cells using QIAshredder Homogenizers and the RNEasy Mini kit
650 (Qiagen) and reverse transcribed to cDNA using the iScript cDNA Synthesis Kit (BioRad) with
651 1µg of RNA template. qRT-PCR was then performed using iQ SYBR Green Supermix run on a
652 CFX384 Touch Real-Time PCR Detection System. To quantify fold expression change, the $\Delta\Delta C_q$
653 method was used to quantify fold expression change by normalizing cycle threshold (C_q) values
654 to housekeeping gene (ACTB) and normalized to control sample (no doxycycline).

655 **Generation of Stably Expressing Doxycycline-Inducible sgRNA Cell Lines**

656 Inducible expression of sgRNAs was achieved using a modified version of the plasmid
657 LentiCRISPR v2 to form a modified all-in-one dox inducible system, namely TLCV2 (Addgene,
658 #87360). Lentivirus particles were produced and cells were transduced as previously described⁶⁸.
659 Following selection with 1ug/mL puromycin for a minimum of seven days, cells were treated with
660 1ug/mL doxycycline for 72 hours prior to flow cytometry-based sorting of the GFP⁺ population.
661 The sorted fraction containing a bulk population of sgRNA-transduced cells was then reintroduced
662 into culture supplemented in media containing 1ug/ml puromycin and 1ug/ml doxycycline for a
663 minimum of 24 hours and a maximum of seven days, during which time cells were used for
664 experimentation.

To generate the *CRBN* knockout cells, OCI-AML2 Cas9 cells were infected with *CRBN*-targeting or non-targeting control guides cloned into pLentiGuide-mTagBFP. Nine days after infection, cells were treated with ARM-165 for 72 hours and analyzed for BFP-positive cells by BD Bioscience Symphony flow cytometer.

Tandem Affinity Purification of PIK3R5/p101 and Proteomics Analysis

Because AML cells cannot sustain ectopic expression of PIK3CG and PIK3R5 over extended culture periods, we employed a doxycycline-inducible vector encoding PIK3R5 for cell transduction. PIK3R5 was chosen due to its smaller size, which facilitated both higher transduction rates and sustained expression using our doxycycline-inducible system. Consequently, OCI-AML2, MV4-11, and NOMO-1 AML cells were transduced with a doxycycline-inducible construct enabling ectopic expression of 3xFlag-HA-PIK3R5. After harvesting, cell pellets were lysed in lysis buffer (100mM KCl, 5mM MgCl₂, 20mM Tris-HCl pH 8, 0.1% Tween 20, 0.1% NP40, 10% glycerol + protease inhibitors) and 1mg of lysate, from each of the four replicates per condition, was used to perform tandem affinity purification. Briefly, lysates were first incubated with anti-flag agarose beads (Sigma-Aldrich, #A2220) for four hours, washed four times with lysis buffer and eluted with 3xflag peptides (Sigma-Aldrich, #F4799). Eluates were then incubated overnight with anti-HA agarose beads and washed three times with lysis buffer and twice with water before digesting them for four hours with 1µg of trypsin prior desalting and MS acquisition. The top-scoring interactors of PIK3R5 were identified based on three criteria: i) showing a significant log₂ fold change enrichment compared to control above 1, ii) displaying specific enrichment in test conditions (no peptides identified in controls), with the number of peptides identified significantly above the mean as defined by z-test, and iii) being identified in at least two out of three cell lines. These PIK3R5 interactors were used to construct a STRINGdb physical interaction network (score > 0.5) to visually represent known interactions.

Whole-Genome CRISPR/Cas9 Screen

shRNA library was amplified and prepared as previously described⁶⁹ using the Toronto Knockout CRISPR Library – Version 3 (TKOv3) obtained from Addgene (Pooled Libraries #90294, #125517). OCI-AML2 cells were transduced at 1000X coverage of the library (72 x 10⁶ cells transduced) and cultured for a minimum of 1000X coverage for the duration of the screen. After 7 days of puromycin selection, cells were divided into three treatment arms – cells treated with DMSO or MK-2206 (1µM) – for two weeks. Genomic DNA was extracted using the DNeasy Blood & Tissue Kit (Qiagen). Amplification of sgRNA barcodes and indexing of each sample was performed via 2-step PCR as described previously⁶⁹. Identification of sensitizing or resistor genes was performed as previously described by comparing the final drug treated populations to DMSO treated⁶⁹.

Tracking of Indels by Decomposition (TIDE) Assay

DNA was extracted from sgRNA infected cells using the Zymoclean™ Gel DNA Recovery Kit (Zymoclean #D4008). The region of interest, encompassing the CRIPR-Cas9-edited region, was amplified from the genomic *PIK3CG* and *PIK3R5* DNA regions. Sequences were amplified in multiple 50µL reactions using Q5 High Fidelity 2X Master (New England BioLabs, #SM0492S). After PCR amplification, samples were cleaned using AMPure XP beads for cleanup (Beckman Coulter, #10136224), and prepared for Sanger sequencing. Non-targeting control sequences were aligned to sg*PIK3CG*/ sg*PIK3R5* sequences to quantify the efficiency of the sgRNA using the TIDE online tool³⁰.

Methylcellulose Assays

AML cell lines were either treated with indicated small-molecule inhibitors or infected with a control, or two *PIK3R5*- and *PIK3CG*-directed sgRNAs. Infected cells were selected with puromycin two days after infection and Cas9 expression was then induced with 1µg/mL doxycycline for three days before the sorting of GFP-positive cells. Sorted cells were then counted

by Trypan blue exclusion, and 1×10^4 cells were plated 1:10 (vol/vol) in methylcellulose (Clona-Cell-TCS Medium #03814) with 1 μ g/ml doxycycline, 1 μ g/ml puromycin and treated with indicated drug concentrations. Primary viable cells (1×10^5 cells/ml) were plated onto semi-solid methylcellulose medium (MethoCult; StemCell Technologies, #04435) and treated with indicated drug concentrations. Cell colonies were evaluated after a minimum of 10 days after plating.

Flow Cytometry

For the detection of GFP-positive *Cbfb-MYH11*-driven or luciferase-expressing OCI-AML2 leukemic cells, bone marrow and spleen were crushed and smashed, respectively, prior to be washed and resuspended in PBS 2mM EDTA, and analyzed on a BD FACSCanto II Instrument (BD Biosciences). For the detection of primary Patient-Derived Xenograft (PDX) cells, peripheral blood was collected from NOG-EXL mice prior to lysis of red blood cells for 10 minutes (Sigma-Aldrich, #R7757), washing, and resuspension of the leukemic cells into PBS 0.1% BSA 2mM EDTA. PDX cells were then stained for 25 minutes at four degrees with PE-Vio770-coupled anti-hCD45 antibody (Miltenyi Biotec, # 130-110-634). Cells were then washed twice with PBS 0.1% BSA 2mM EDTA, and analyzed on a BD FACSCanto II Instrument (BD Biosciences). The cell gating strategy is shown in **Figures S10** and **S11**.

Annexin V5 Detection

Annexin V staining was performed using the eBioscience™ Annexin V Apoptosis Detection Kits per the manufacturer's protocol (Thermofisher #88-8007-74). Treated cell lines were diluted with 1X binding buffer to 1 million cells per mL before they were stained with Annexin V APC (1:20 dilution) for 10 -15 minutes at room temperature. Cells were washed with 1X of binding buffer. Cells were resuspended with 200uL of 1X binding buffer and immediately analyzed on BD FACScanto II (BD Biosciences).

Generation of Luciferase-Expressing OCI-AML2 Cells

OCI-AML2 cells were transduced with pMMP-LucNeo retrovirus and selected with 1mg/mL neomycin. These cells were then transduced with lentiviral particles encoding either a non-targeting control or *PIK3CG*-directed sgRNAs, and then selected for seven days with 1µg/mL puromycin and then used for subsequent *in vivo* studies.

***In Vivo* Imaging**

After a minimum of six days post-injection of bioluminescent cells, mice were injected with 150mg/kg luciferin (Xenolight, #12799) 15 minutes prior to imaging, anesthetized with 2-4% isoflurane, and imaged, using the IVIS Lumina III according to the manufacturer's protocol. Bioluminescent signal was quantified in ph. s⁻¹. cm⁻². sr⁻¹ using a standardized region of interest (ROI) encompassing the entire mouse.

***In Vivo* Genetic Studies**

Luciferase-expressing OCI-AML2 cells were infected with non-targeting control or *PIK3CG*-directed sgRNAs, selected with puromycin; the GFP-positive cell fraction was sorted as described above. Following sorting, cells were allowed to recover in media supplemented with 1µg/mL doxycycline and 1µg/m puromycin for four days. 6-week-old male NSG mice (NOD.Cg.Prkdc ^{scid} Il2rg^{tm1Sug}Tg(SV40/HTLV-IL-3, CSF2)10-7jic Taconic) were then irradiated at 1.25 Gy and injected with 1 x10⁶ cells per mouse by intravenous injection. These mice were supplemented with doxycycline-containing food (SAFE nutrition service, #E8200P01R) for the whole duration of the experiment. Imaging of the mice was performed every three days to follow the disease progression. Peripheral blood was collected by submandibular bleeding and bone marrow biopsies were performed on mice femurs to collect bone marrow mononuclear cells. Either, at the end point, mice were euthanized, and spleen and bone marrow harvested. The GFP-positive AML cell fraction was quantified in both bone marrow and spleen on a BD FACSCanto II Instrument (BD Biosciences).

For survival studies, mice were monitored for signs of distress, such as weakness, weight loss, ruffled coat, lethargy or bruising. Observance of humane endpoints as described in our protocol—loss of body weight > 15% free-feeding body weight, inability to rise or ambulate, presence of labored respiration, wound ulceration, or other signs of active infection—resulted in euthanization. As this study pertains to leukemia, a maximal tumor size was not enforced. Drug treatments and routine monitoring continued for 52 days or until a humane endpoint was reached.

In vivo Drug Treatment Studies

Cbfb-MYH11 Syngeneic Mouse Model: The *Cbfb-MYH11*-driven leukemic cells were kindly provided by Dr. Lucio U. Castilla's team. Those were isolated from the offspring of floxed *Cbfb-MYH11* knock-in mice which were crossed with the *Mx1-Cre* transgenic mice⁷⁰. 0.5×10^6 *Cbfb-MYH11* cells were injected into 5- to 8- week-old male C57BL/6J mice (Envigo). Seven days after injection, a biopsy of the bone marrow was performed to confirm disease engraftment and mice were randomized to ensure homogenous disease onset across animals prior to the start of the treatment.

Patient-Derived Xenograft (PDX) Mouse Model: The PDX sample was derived from a 69-year-old female who was diagnosed with secondary AML with MDS-related changes; the genetic profiling of this patient revealed mutations in *CEBPA/ ASXL1/ RUNX1/ EZH2/ JAK2/ TET2*; patient karyotype is 46, XX , t(6;7)(q23;q11.2)[1]/46,XX[cp19]. 1×10^6 mononucleated cells were injected via the tail vein into sublethally-irradiated (1.25Gy) 8-week-old NOG-EXL mice (Taconic Biosciences). Blast engraftment was confirmed by flow cytometry one month after injection using the PE-Vio770-coupled CD45 (hCD45)-based staining protocol detailed in the flow cytometry section to confirm disease engraftment and mice were randomized accordingly.

Venetoclax was administered daily at a dosage of 100mg/kg by oral gavage (in 5% DMSO; 40% PEG300, 5% TWEEN80, 50% Saline), AZ2 and ARM165 were administered daily until mice

demise at 0.051mg/kg by IV injection (in 20% *N*-methylpyrrolidone EMPLU, #8060721000, Sigma-Aldrich; 16% PEG400, 64% saline solution). At indicated time points response to treatment was tracked using either peripheral mandibular bleeding and bone marrow biopsy. 14 days after cell injection, mice were euthanized, bone marrow and spleen were harvested, weighted and the GFP-positive leukemic cell fraction was quantified using a BD FACSCanto II Instrument (BD Biosciences).

***In vivo* Toxicity Studies**

Naïve C57BL/6 mice were treated with ARM165 at 0.051mg/kg by IV injection (in 20% *N*-methylpyrrolidone EMPLU, # 8060721000, Sigma-Aldrich; 16% PEG400, 64% saline solution) or Vehicle alone for 5 days and toxicity was evaluated via weight measurement and characterization of hematopoietic cell compartment. Mice were monitored for signs of toxicity through measurement of body weight over 7 consecutive days or on day 5 by FACS analysis of the hematopoietic cell compartment. Blood was collected and hematopoietic populations were characterized using a MS9-5 machine as per the manufacturer's protocol. Bone marrow and spleen were collected and processed with antibodies listed below to analyze each hematopoietic stem, progenitor, or mature cell fractions in bone marrow, and granulomonocytic and B- and T-cell fractions in spleen.

Target	Provider	Reference
Lin ^{Low} (APC)	BD	51-9003632
Sca-1 (PeCy7)	Thermo Fisher Scientific	17-5931-82
Cd117 (PE)	Thermo Fisher Scientific	12-1172-83
Cd34 (Pacific Blue)	Thermo Fisher Scientific	48-0341-82
Cd16/32 (Per-CP)	Thermo Fisher Scientific	45-0161-82
Cd41 (Pacific Blue)	Biolegend	133932
Ter119 (FITC)	Biolegend	116206
Gr1 (APC)	Thermo Fisher Scientific	17-5931-81
Cd11b (PeCy7)	Thermo Fisher Scientific	25-0112-82
Cd8a (Pecy7)	Thermo Fisher Scientific	A15385
B220 (APC)	Thermo Fisher Scientific	17-0452-82

RNA-sequencing Analysis

For RNA-sequencing analysis, total RNA was extracted from MOLM-14 and OCI-AML2 cells treated with either DMSO, 0.5 μ M or 1 μ M AZ2 or ARM165, respectively, for 24 hours using RNAeasy plus mini kit following manufacturer's instruction. Sequencing libraries were prepared using TruSeq Stranded mRNA LT Sample Prep Kit (Illumina) and 151bp paired-end sequencing on a NovaSeq6000 (Illumina) at MacroGen Europe (Amsterdam, The Netherlands). The total number of reads for individual samples ranged from 134 million to 217 million with at least 94% of reads >Q30. Quality-control tests for the unmapped reads were performed using the FASTQC software (<http://www.bioinformatics.babraham.ac.uk/projects/fastqc/>). Sequencing reads were pseudo aligned to the ENSEMBL GRCh38 version of the human genome and abundance quantified using Kallisto (<https://pachterlab.github.io/kallisto/>). Differential expression analysis was done using the Sleuth R package⁷¹. PCA plots and heatmap were plotted using R packages ggplot2 and pheatmap.

Overrepresentation Analysis

A list of the top 2928 commonly up-regulated and 2756 commonly down-regulated genes (based q-value < 0.001 by sleuth analysis) between the control and ARM165-treated conditions, was selected across the two AML cell lines for overrepresentation analysis. Over-representation analysis was performed in R v4.2.2 using genekitr package v1.2.2 using MSigDB HALLMARK and C2 geneset libraries.

Single Sample Gene Set Enrichment (ssGSEA) Analysis

Single-sample GSEA (ssGSEA) was used to calculate separate enrichment scores for each sample whose transcriptomic data was available from BEAT-AML (n=451 patients) and gene sets (queried from the MSigDB Hallmark and C2 and ARM165 downregulated gene signature). The top 149 common downregulated genes in the two AML cell lines treated with

ARM165 was retained for ssGSEA analysis. ssGSEA was computed in R with GSVA v1.48.3 package using the following parameters: method="zscore", abs.ranking=FALSE, min.sz=2, max.sz=Inf, parallel.sz=18, mx.diff=TRUE, tau=switch(method, gsva=1, ssgsea=0.25, NA), ssgsea.norm=TRUE.

PIK3CG expression patient stratification: Gene expression data of AML patients whose transcriptomic profiling was available from the BEAT AML cohort (n=451)²⁷, were z-score normalized and high versus low *PIK3CG* levels were evaluated based on the absolute z-score cut-off of 0.7. On versus off ARM165 signatures were assigned for each patient based on a normalized enrichment score below or above the median score across the whole cohort. The significance of the differences between the proportions of each subgroup of patients was evaluated by applying the two tailed Fisher's Exact Test.

Associations Between Genetic and Clinical Features and *PIK3CG* and *PIK3R5* Levels

For BEAT-AML RNAseq analysis, we used STAR counts and clinical annotation from BEAT AML 1.0 cohort²⁷. Gene expression from AML diagnosis and relapse samples were normalized using the median of ration method, using DESeq2 package. Single-sample cell type signatures^{28,29} were calculated using the gsva package⁷². Differences between *PIK3CG/PIK3R5* gene expression and cytologic/genetic groups were tested using a Wilcoxon test, and correlations with transcriptomic signatures and drug sensitivity AUC were tested using Spearman correlation.

Protein Abundance Analysis

Pellets from HEK293T expressing *PIK3CG* with or without treatment of 2 μ M of ARM165 for 24 hours were lysed in 8M urea + 25mM ammonium bicarbonate (ABC) followed by reduction (5mM DTT for 1hr at 37C) and alkylation (10mM iodoacetamide for 30min at RT in the dark) of 200ug of proteins per samples. The samples were diluted 8-fold with 25mM ABC and digested overnight with 2ug of trypsin (Promega). After acidification with TFA to a final concentration of

0.5%, samples were desalted using UltraMicroSpin C18 columns (The Nest Group). The columns were activated with 200 μ L of 80% acetonitrile (ACN) and 0.1% TFA and equilibrated three times with 200 μ L of 0.1% TFA. Peptide samples were applied to the columns, and the columns were washed three times with 200 μ L of 0.1% TFA. Peptides were eluted with 140 μ L of 50% ACN and 0.25% formic acid and lyophilized. Samples were resuspended in 0.1% formic acid and separated by reverse phase using a Vanquish Neo HPLC (Thermo Scientific) using 15 cm long PepSep column with a 150 μ m inner diameter packed with 1.5 μ m Reprosil Saphir C18 particles (Bruker). Samples were acquired by DDA (2 untreated and 2 ARM165 samples to build spectral library) and DIA (all 4 replicates per conditions) methods. Mobile phase A consisted of 0.1% FA in water and mobile phase B consisted of 80% acetonitrile (ACN)/0.1% FA. Peptides were separated at a flow rate of 500 nL/min by the following 80min gradient: 3%–24% B over 60 min; 24%–40% B over 10 min; and 10 min at 95% B. Eluting peptides were analyzed by an Orbitrap Exploris Mass Spectrometer (Thermo Scientific). Data were collected in positive ion mode with MS1 detection in profile mode in the orbitrap using 120,000 resolution, 350–1,150 m/z scan range, auto maximum injection, and a normalized AGC target of 300 (%). For DDA acquisitions, MS2 fragmentation was performed on charge states from 2 to 6, MIPS mode = peptide, with a 30-s dynamic exclusion after a single selection, and 10 ppm \pm mass tolerance. All raw MS data were searched using Spectronaut (v 18.4.231017.55695) against the human proteome (Uniprot canonical protein sequences downloaded September, 2022) using default settings for spectral library generation and DIA analysis.

Chemistry

General considerations:

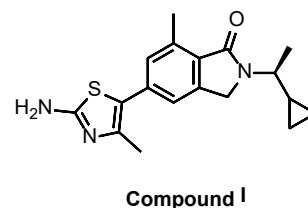
All organic solvents were purchased from commercial sources and used as received. All chemicals were purchased from Merck, IRIS Biotech, BLDPharm and used without further purification. ^1H and $^{13}\text{C}\{^1\text{H}\}$ NMR spectra were recorded on a Bruker 400 or 500 MHz

spectrometer; chemical shifts are given in ppm and referenced to the solvent residual peak (CDCl₃: 7.16 ppm for ¹H and 77.16 for ¹³C; DMSO-d₆: 2.50 ppm for ¹H and 39.52 for ¹³C), coupling constants are given in Hertz (Hz). The purity of the final compounds (ARM165 and ARM204) was verified to be ≥ 95 % purity by UPLC analysis at 214 nm on a Waters Acquity H-Class system equipped with a UV detector, SQD2 mass spectrometer detector and an acquity HSS T3 column (100Å, 1.8 µm, 2.1 mm × 50 mm; gradient water/acetonitrile (1‰ formic acid): 100/0 to 0/100 in 5 min; flow: 0.8 mL/min). Preparative HPLC were performed either on Gilson PLC2250 using a C18-reverse phase (DeltaPack Waters, 15 µm, 100Å, 100 × 40 mm) or a GILSON HPLC system – SKID LC 009SK equipped with a C18 reversed-phase Luna column (Phenomenex 15 µm, 100Å, 250 × 50 mm). On the Gilson PLC2250 equipped with DeltaPack, elution was performed using gradients of acetonitrile in water, and a constant concentration 0.1 vol.% of trifluoroacetic acid (TFA) and a 50 mL/min flow rate. On the GILSON HPLC system – SKID LC 009SK equipped with a C18 reversed-phase Luna column, elution was performed using gradients of acetonitrile in water, and a constant concentration 0.1 vol.% of Formic acid and a 120 mL/min flow rate. Docking of AZ2 in PIK3CG was performed on the Alphafold structure of human PIK3CG (Uniprot P48736) using Autodock Vina and the following grid parameters on a rigid receptor: centre x, y, z: 18.701, 19.536, -3.725 and size x, y, z: 21.75, 21.75, 21.75⁷³.

Synthesis of N¹-(5-(2-((S)-1-cyclopropylethyl)-7-methyl-1-oxoisindolin-5-yl)-4-methylthiazol-2-yl)-N⁵-(8-((2-(2,6-dioxopiperidin-3-yl)-1,3-dioxoisindolin-4-yl)amino)-8-oxooctyl)glutaramide (ARM165, Figure S6) and N¹-(5-(2-((S)-1-cyclopropylethyl)-7-methyl-1-oxoisindolin-5-yl)-4-methylthiazol-2-yl)-N⁵-(8-((2-(1-methyl-2,6-dioxopiperidin-3-yl)-1,3-dioxoisindolin-4-yl)amino)-8-oxooctyl)glutaramide (ARM204, Figure S7B):

1- Preparation of Compound I ((S)-5-(2-amino-4-methylthiazol-5-yl)-2-(1-cyclopropylethyl)-7-methylisindolin-1-one)

Synthesis: To a solution AZ2 (cas #: 2231760-33-9; 1.0 g, 2.71 mmol, 1.0 equiv.), in methanol (10 mL) at room temperature, was added a solution of lithium hydroxide monohydrate (1.14 g, 27.1 mmol, 10 equiv.) in water (10 mL). Thereafter, the reaction mixture

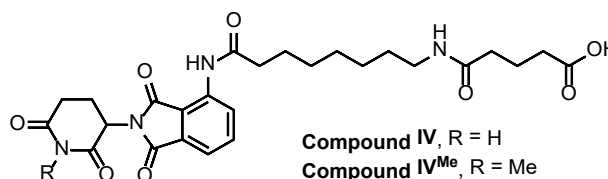


was stirred at 60°C complete consumption of the starting material (LC monitoring, ca. 40 h). The reaction mixture was then concentrated to remove the methanol and diluted with ethyl acetate (100 mL). This organic layer was successively washed with a saturated aqueous solution of sodium bicarbonate and brine, before being dried over magnesium sulphate, filtered, and concentrated to dryness. The title compound was obtained as a beige solid in a 94% yield (834 mg) without further purification.

Characterization: ^1H NMR (CDCl_3 , 400 MHz) δ 7.25 (s, 1H), 7.17 (s, 1H), 5.02 (s, 2H), 4.49 (d, J = 17.0 Hz, 1H), 4.38 (d, J = 17.0 Hz, 1H), 3.75 (dq, J = 9.4, 6.8 Hz, 1H), 2.73 (s, 3H), 2.33 (s, 3H), 1.33 (d, J = 6.8 Hz, 3H), 1.04 – 0.98 (m, 1H), 0.64 – 0.60 (m, 1H), 0.44 – 0.37 (m, 1H); $^{13}\text{C}\{^1\text{H}\}$ NMR (CDCl_3 , 101 MHz) δ 168.5, 165.4, 144.5, 142.6, 137.9, 135.4, 130.5, 129.0, 121.0, 120.4, 51.9, 45.5, 18.6, 17.4, 16.5, 16.1, 4.7, 3.6; MS (ESI+): m/z 328.3 $[\text{M}+\text{H}]^+$ (100%).

2- Preparation of Compound IV (5-((8-((2-(2,6-dioxopiperidin-3-yl)-1,3-dioxoisindolin-4-yl)amino)-8-oxooctyl)amino)-5-oxopentanoic acid):

Synthesis: A) To a solution of pomalidomide (cas #: 19171-19-8, 1.0 g, 3.65 mmol, 1.0 equiv.), and Boc-AOc-OH (8-[(tert-butoxycarbonyl)amino]octanoic acid, cas #: 30100-16-4, 0.95 g, 3.65 mmol, 1.0 equiv.) in



N,N -dimethylformamide (25 mL) and pyridine (3.0 mL, 36.5 mmol, 10 equiv.) at room temperature, was added a solution of T3P (2,4,6-tripropyl-1,3,5,2,4,6-trioxatriphosphorinane) 50 wt.% in ethyl acetate (cas # 68957-94-8, 10.8 mL, 18.25 mmol, 5.0 equiv.). Then, the reaction mixture was

925 allowed to stir at 80°C during 16 h. Next, the volatiles were evaporated off and the oily residue
926 dissolved in 100 mL of ethyl acetate. This organic layer was successively washed with a saturated
927 aqueous solution of sodium bicarbonate and brine, before being dried over magnesium sulphate,
928 filtered, and concentrated to dryness. The crude Compound II was directly engaged in the
929 subsequent step.

930 B) Crude Compound II (1.46 mmol) was dissolved in 5 mL of anhydrous *N,N*-
931 dimethylformamide, at room temperature, and reacted with methyl iodide (120 µL, 1.90 mmol, 1.3
932 equiv.) in the presence of potassium carbonate (260 mg, 1.90 mmol, 1.3 equiv.) during 16 h. After
933 concentration to dryness, the residue was dissolved in 100 mL of ethyl acetate and successively
934 washed with KHSO₄ aq. (1 M solution, twice), a saturated aqueous solution of sodium bicarbonate
935 and brine. Thereafter, the organic layer was dried over magnesium sulphate, filtered, and
936 concentrated to dryness. The crude Compound II^{Me} was directly engaged in the subsequent step.

937 C) This step was separately performed on Crude Compound II (3.65 mmol) and
938 Crude Compound II^{Me} (1.46 mmol) as the starting materials. The starting material was dissolved
939 in 15 mL of dichloromethane and treated with trifluoroacetic acid (8 mL) at room temperature
940 during 2 h. After concentration to dryness and lyophilisation from a 1/1 mixture of
941 acetonitrile/water, the corresponding Compound III or Compound III^{Me} was obtained as a
942 trifluoroacetate salt in a light orange solid form and directly engaged in the next step.

943 D) This step was separately performed on Crude Compound III (3.65 mmol) and
944 Crude Compound III^{Me} (1.46 mmol) as the starting materials. The starting material (1.0 equiv.)
945 was dissolved in 20 mL of *N,N*-dimethylformamide and 20 mL of toluene. To this mixture, *N,N*-
946 diisopropylethylamine (3.0 equiv.) and glutaric anhydride (1.1 equiv.) were successively added
947 and the media was allowed to stir at 110°C for 2 h. Thereafter, the volatiles were evaporated off
948 and the residue resuspended in a 1/1 mixture of acetonitrile/water prior to its lyophilization.
949 Purification of Compound IV: the lyophilized crude product (2.6 g) was solubilized in

water/acetonitrile 35/65 (v/v) mixture with 1‰ Formic acid (FA) (20 ml), filtered on a 0,45 µm syringe filter and purified by RP-preparative HPLC. The purification was performed on a GILSON HPLC system – SKID LC 009SK - equipped with a C18 reversed-phase Luna column (Phenomenex 15 µm, 100Å, 250 × 50 mm) with a flow rate of 120 mL/min. Eluents were water 1‰ FA (A) and acetonitrile 1‰ FA (B). The purification is carried out according to the following gradient: From 0% to 20% of B in 5 minutes then from 20% to 30% of B in 5 minutes and finally, from 30% to 45% of B in 15 minutes. The compound of interest is eluted in 19 minutes. UV detection was performed at 214 nm. Collected fractions were concentrated and freeze-dried to obtain 1.2 g of pure Compound IV as a colourless solid in a 62% overall yield (3 steps).

Characterization of Compound IV: ¹H NMR (DMSO-*d*₆, 500 MHz) δ 12.01 (s, 1H), 11.14 (s, 1H), 9.69 (s, 1H), 8.49 – 8.46 (m, 1H), 7.82 (dd, *J* = 8.4, 7.3 Hz, 1H), 7.74 (t, *J* = 5.6 Hz, 1H), 7.61 (dd, *J* = 7.3, 0.7 Hz, 1H), 5.15 (dd, *J* = 12.9, 5.4 Hz, 1H), 3.01 (q, *J* = 6.9 Hz, 2H), 2.90 (ddd, *J* = 17.1, 13.9, 5.5 Hz, 1H), 2.64 – 2.51 (m, 2H), 2.46 (t, *J* = 7.5 Hz, 2H), 2.18 (t, *J* = 7.4 Hz, 2H), 2.09 – 2.04 (m, 3H), 1.69 (p, *J* = 7.5 Hz, 2H), 1.65 – 1.59 (m, 2H), 1.40 – 1.23 (m, 3H); ¹³C{¹H} NMR (DMSO-*d*₆, 126 MHz) δ 174.2, 172.8, 172.0, 171.3, 169.8, 167.7, 166.7, 136.6, 136.1, 131.5, 126.3, 118.3, 117.0, 48.9, 38.4, 36.5, 34.5, 33.0, 30.9, 29.1, 28.5, 28.5, 26.3, 24.7, 22.0, 20.7; MS (ESI+): *m/z* 529.3 [M+H]⁺ (100%).

Purification of Compound IV^{Me}: the lyophilized crude product (0.8 g) was solubilized in water/acetonitrile 70/30 (v/v) mixture with 1‰ TFA (25 ml), filtered on a 0,45 µm syringe filter and purified by RP-preparative HPLC on a PLC2250 Gilson system equipped with a DeltaPack Waters column (15 µm, 100Å, 100 × 40 mm) and a UV detector at 214 nm. Elution was performed using gradients of acetonitrile (B) in water (A), at a constant concentration 1‰ TFA, and a flow rate of 50 mL/min. The following stepwise gradient was applied: 100% A to 85/15 A/B in 3 min., 85/15 to 75/25 A/B in 5 min., and 75/25 to 45/55 A/B in 30 min. The product is eluted out at 45% of B.

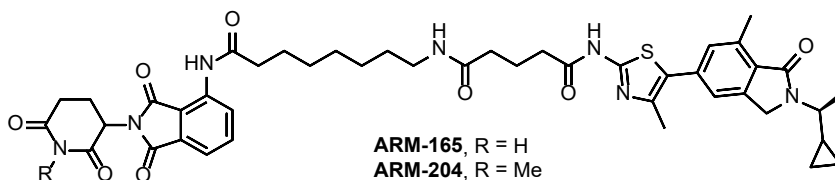
Collected fractions were freeze-dried to obtain 432 mg of pure Compound IV^{Me} as a colourless solid in a 54% overall yield (4 steps).

Characterization of Compound IV^{Me}: ¹H NMR (DMSO-*d*₆, 400 MHz) δ 9.68 (s, 1H), 8.48 (dd, *J* = 8.5, 0.8 Hz, 1H), 7.83 (dd, *J* = 8.4, 7.3 Hz, 1H), 7.74 (t, *J* = 5.6 Hz, 1H), 7.61 (dd, *J* = 7.3, 0.8 Hz, 1H), 5.21 (dd, *J* = 13.0, 5.4 Hz, 1H), 3.03 – 2.92 (m, 6H), 2.78 (ddd, *J* = 17.2, 4.5, 2.6 Hz, 1H), 2.61 – 2.53 (m, 1H), 2.45 (t, *J* = 7.4 Hz, 2H), 2.18 (t, *J* = 7.4 Hz, 2H), 2.11 – 2.05 (m, 3H), 1.73 – 1.65 (m, 2H), 1.65 – 1.58 (m, 2H), 1.41 – 1.22 (m, 8H); ¹³C{¹H} NMR (DMSO-*d*₆, 101 MHz) δ 174.2, 172.0, 171.7, 171.3, 169.5, 167.7, 166.6, 136.6, 136.1, 131.4, 126.3, 118.3, 116.9, 49.5, 38.4, 36.5, 34.5, 33.0, 31.1, 29.1, 28.5, 28.4, 26.6, 26.3, 24.7, 21.2, 20.7; MS (ESI⁺): *m/z* 543.3 [M+H]⁺ (100%).

3- Preparation of ARM165 N¹-(5-(2-((S)-1-cyclopropylethyl)-7-methyl-1-oxoisindolin-5-yl)-4-methylthiazol-2-yl)-N⁵-(8-((2-(2,6-dioxopiperidin-3-yl)-1,3-dioxoisindolin-4-yl)amino)-8-oxooctyl)glutaramide and ARM204 N¹-(5-(2-((S)-1-cyclopropylethyl)-7-methyl-1-oxoisindolin-5-yl)-4-methylthiazol-2-yl)-N⁵-(8-((2-(1-methyl-2,6-dioxopiperidin-3-yl)-1,3-dioxoisindolin-4-yl)amino)-8-oxooctyl)glutaramide (Figures S6 and S7B)

Synthesis: Compound I, (1.0 equiv.), and Compound IV (1.0 equiv.) for the preparation of ARM165, or Compound

IV^{Me} (1.0 equiv.) for the preparation of ARM204,



were dissolved in 1 mL of *N,N*-dimethylformamide and *N,N*-diisopropylethylamine (5.0 equiv.). Then, HATU (Hexafluorophosphate Azabenzotriazole Tetramethyl Uronium, 1.0 equiv.) was added and the mixture was allowed to stir at room temperature for 6 h before an additional portion of 0.2 equiv. of HATU was introduced. After 16 h, without any treatment, the reaction media was purified on reverse phase preparative HPLC – PLC2250 Gilson (DeltaPack Waters, 15 μm, 100Å,

998 100 × 40 mm). Of note, ARM165 and ARM204 were prepared on a 0.37 mmol and 73 μmol scale,
999 respectively.

1000 Purification: in both cases, elution was performed using gradients of acetonitrile (B) in
1001 water (A), at a constant concentration 0.1 vol.% of TFA, and a flow rate of 50 mL/min. The
1002 following stepwise gradient was applied: 100% water (A), 0% acetonitrile (B) during 3 min., 100%
1003 A to 65/35 A/B in 7 min., 65/35 to 55/45 A/B in 5 min., and 55/45 to 35/65 A/B in 20 min. The
1004 product is eluted out at 55% of B (ARM165), or 58% of B (ARM204). The title compounds ARM165
1005 and ARM204 were obtained as colourless solids in a 55% and 29% yield, respectively.

1006 Characterization of ARM165: ¹H NMR (CDCl₃, 400 MHz) δ 9.42 (s, 1H), 8.79 (d, *J* = 8.5
1007 Hz, 1H), 8.38 (s, 1H), 7.70 (dd, *J* = 8.5, 7.3 Hz, 1H), 7.53 (dd, *J* = 7.3, 0.7 Hz, 1H), 7.30 (s, 1H),
1008 7.22 (s, 1H), 6.28 (t, *J* = 5.8 Hz, 1H), 4.98 – 4.93 (m, 1H), 4.56 (d, *J* = 17.5 Hz, 1H), 4.45 (d, *J* =
1009 17.4 Hz, 1H), 3.76 (dq, *J* = 9.4, 6.8 Hz, 1H), 3.29 (q, *J* = 6.7 Hz, 2H), 2.94 – 2.75 (m, 6H), 2.69 (t,
1010 *J* = 7.2 Hz, 2H), 2.51 (s, 3H), 2.48 (t, *J* = 7.3 Hz, 2H), 2.34 (t, *J* = 7.2 Hz, 2H), 2.20 – 2.17 (m, 1H),
1011 2.11 (p, *J* = 7.1 Hz, 2H), 1.77 (p, *J* = 7.3 Hz, 2H), 1.58 (p, *J* = 7.2 Hz, 2H), 1.47 – 1.41 (m, 2H),
1012 1.35 (d, *J* = 6.8 Hz, 3H), 1.07 – 0.98 (m, 1H), 0.69 – 0.63 (m, 1H), 0.50 – 0.34 (m, 3H); ¹³C{¹H}
1013 NMR (CDCl₃, 126 MHz) δ 172.6, 172.3, 172.2, 171.2, 169.4, 169.3, 168.3, 166.9, 157.0, 142.7,
1014 138.1, 137.9, 136.6, 134.3, 131.3, 130.8, 129.8, 125.6, 125.1, 120.7, 118.7, 115.5, 52.0, 49.4,
1015 45.5, 39.6, 38.0, 35.1, 35.0, 31.6, 29.7, 28.7, 28.6, 26.5, 25.3, 23.0, 21.2, 18.7, 17.5, 16.0, 15.6,
1016 4.7, 3.6; MS (ESI+): *m/z* 838.5 [M+H]⁺ (87%), 419.9 [M+2H]²⁺ (100%); HPLC (λ₂₁₄) 97 % purity.

1017 Characterization of ARM204: ¹H NMR (CDCl₃, 400 MHz) δ 9.44 (s, 1H), 8.81 (d, *J* = 7.7
1018 Hz, 1H), 7.70 (dd, *J* = 8.5, 7.3 Hz, 1H), 7.54 (dd, *J* = 7.3, 0.8 Hz, 1H), 7.31 (s, 1H), 7.23 (s, 1H),
1019 6.26 (t, *J* = 6.0 Hz, 1H), 4.96 (dd, *J* = 12.2, 5.8 Hz, 1H), 4.57 (d, *J* = 17.5 Hz, 1H), 4.46 (d, *J* =
1020 17.5 Hz, 1H), 3.77 (dq, *J* = 9.2, 6.8 Hz, 1H), 3.26 (q, *J* = 6.9 Hz, 2H), 3.22 (s, 3H), 3.06 – 2.95 (m,
1021 1H), 2.84 – 2.75 (m, 5H), 2.70 (t, *J* = 7.2 Hz, 2H), 2.52 (s, 3H), 2.46 (t, *J* = 7.5 Hz, 2H), 2.37 (t, *J*
1022 = 7.3 Hz, 2H), 2.15 – 2.08 (m, 3H), 1.75 (p, *J* = 7.1 Hz, 2H), 1.52 (p, *J* = 7.5 Hz, 2H), 1.41 – 1.32

1023 (m, 9H), 1.07 – 0.98 (m, 1H), 0.70 – 0.63 (m, 1H), 0.50 – 0.33 (m, 3H); $^{13}\text{C}\{^1\text{H}\}$ NMR (CDCl_3 , 126
1024 MHz) δ 173.2, 172.7, 172.0, 171.1, 169.5, 168.7, 168.2, 167.0, 160.3, 143.2, 139.2, 137.9, 136.5,
1025 133.5, 131.4, 131.3, 131.2, 130.8, 125.4, 125.0, 120.8, 118.6, 115.5, 52.5, 50.2, 45.7, 40.1, 38.0,
1026 35.4, 35.2, 32.0, 29.4, 29.0, 28.9, 27.5, 26.7, 25.2, 22.2, 21.1, 18.6, 17.5, 16.0, 13.1, 4.8, 3.7; MS
1027 (ESI+): m/z 852.5 $[\text{M}+\text{H}]^+$ (52%), 426.8 $[\text{M}+2\text{H}]^{2+}$ (100%); HPLC (λ_{214}) 98 % purity.

1028 **Data Availability**

1029 Gene expression data for normal and malignant tissues was obtained from the GeTex
1030 gene expression dataset and accessed via the Gepia portal. Gene dependency data was obtained
1031 from the DepMap dependency dataset. Data analyses were performed using R or
1032 GraphPad/Prism 8. Raw counts from the BEAT AML 1.0 cohort were available from the NIH GDC
1033 portal, and genetic and clinical annotations were available from the supplementary information
1034 provided in the original article reporting this cohort²⁷. TCGA data were available from the NIH GDC
1035 portal. The RNA-sequencing-based profiling of the AML cell lines treated with ARM165 is
1036 available from GSE260759. Additional data that support the findings of this study are available
1037 from the co-corresponding authors upon reasonable request.

1038 **Statistical Analysis**

1039 Determination of statistical significance using Microsoft Excel and Prism 8.0.1
1040 (GraphPad); unpaired student's T-test was applied where data was normally distributed. Where
1041 data variance was high, we applied Welch's correction to analyze significance, and pairwise
1042 comparison of data which was not normally distributed was analyzed using non-parametric Mann-
1043 Whitney test. Multiple comparison analysis testing was achieved using the one-way ANOVA test
1044 and the mean of each condition was compared with the mean of every other column.
1045 Bioluminescence imaging testing was achieved using two-way ANOVA test across the different
1046 assessed time points. Associations between *PIK3CG/PIK3R5* gene expression and

1047 cytologic/genetic groups were tested using Wilcoxon test, and correlation studies were carried out
1048 using Spearman correlation. The level of significance was set at 0.05.

1049 **AUTHORS CONTRIBUTION**

1050 L.M.K.: conceptualization, formal analysis, validation, investigation, visualization, methodology,
1051 writing-original draft. J.C.R.: conceptualization, formal analysis, validation, investigation,
1052 visualization, methodology. K.H.L.: conceptualization, formal analysis, validation, investigation,
1053 visualization, methodology. F.L.: investigation, methodology. M.D.: resources, investigation. E.L.:
1054 investigation, methodology. N.A.: investigation, methodology. H.P.: resources, methodology.
1055 D.HN.: investigation, methodology. J.C.: investigation. S.T.K.: investigation, H.X.A: investigation.
1056 F.N.: investigation. C.C.: resources. B.L.: methodology. D.L.: methodology. L.B.: methodology,
1057 resources. E.C.: methodology, resources. P.V.: methodology, resources. M.A.: methodology,
1058 resources. S.F.: resources. T.H.: resources. M.S.: resources. L.A.: resources. E.R.: resources.
1059 N.F.: methodology, resources, support. R.I.: conceptualization, methodology, investigation. C.L.:
1060 conceptualization, formal analysis, visualization, methodology. L.Be.: conceptualization,
1061 investigation, methodology, resources. A.F.: conceptualization, investigation, methodology,
1062 visualization. A.R.M.: conceptualization, formal analysis, supervision, investigation, visualization,
1063 methodology, writing-original draft. K.C.W.: conceptualization, supervision, funding acquisition,
1064 investigation, visualization, methodology, writing-original draft, project administration. A.P.:
1065 conceptualization, formal analysis, supervision, funding acquisition, investigation, methodology,
1066 writing-original draft, project administration.

ACKNOWLEDGMENTS

1067 We thank the members of the A. Puissant, K. C. Wood, and A. R. Martin laboratories for
1068 their scientific input. We are indebted to Veronique Montcuquet, Nicolas Setterblad, Christelle
1069 Doliger, Claire Maillard from the Saint-Louis Research Institute Core Facility, and CNRS,

University Montpellier and SynBio3 platform supported by IBiSa & Chimie Balard Cirimat Carnot Institute. We are grateful to Dr. Lucio H. Castilla for providing us with the *Cbfb-MYH11* knock-in mouse model and to Pr. Matthias Wymann for providing us with the *PIK3CG*-directed antibody and for fruitful suggestions on the project. This work was supported by the ERC Starting and Consolidator programs (758848 and 101088563, to A.P.), the Laurette Fugain association (to A.P.), Amgen Innovations (to A.P.), Fondation ARC (to C.Lo.), ATIP-Avenir 2022 - Ligue Nationale contre le Cancer (to L. Be.), and the INCA PLBIO program (PLBIO20-246, to A.P. and C.Lo., PLBIO20-074, to C.Lo.). This work was supported by NIH R01CA266389 (to K.C.W. and A.P.). This work was supported by NIH 5U54CA274502-02 (to A.F., D.L.S., and N.J.K.). M.D. is supported by the Bettencourt-Schueller Foundation (CCA-INSERM-Bettencourt). A. P. is a FSER laureate and a recipient of the Brigitte Mérand, Jean Valade and Tourre awards. A.P., R.I., L.Be., C.L. are supported by the SIRIC InsiTu program (INCa-DGOS-INSERM-ITMO Cancer_18008).

COMPETING INTERESTS

The Krogan Laboratory has received research support from Vir Biotechnology, F. Hoffmann-La Roche, and Rezo Therapeutics. N.J.K. has financially compensated consulting agreements with the Icahn School of Medicine at Mount Sinai, New York, Maze Therapeutics, Interline Therapeutics, Rezo Therapeutics, GEn1E Lifesciences Inc., and Twist Bioscience Corp. He is on the Board of Directors of Rezo Therapeutics and is a shareholder in Tenaya Therapeutics, Maze Therapeutics, Rezo Therapeutics, and Interline Therapeutics. K.C.W. is a co-founder, consultant, and equity holder at Tavros Therapeutics and Celldom, is a consultant and equity holder at Simple Therapeutics and Decrypt Biomedicine, and has performed consulting work for Guidepoint Global, Bantam Pharmaceuticals, and Apple Tree Partners. The remaining authors declare no competing interests.

REFERENCES

- 1093 1 Shimony, S., Stahl, M. & Stone, R. M. Acute myeloid leukemia: 2023 update on diagnosis,
1094 risk-stratification, and management. *American journal of hematology* **98**, 502-526,
1095 doi:10.1002/ajh.26822 (2023).
- 1096 2 Appelbaum, F. R. *et al.* Age and acute myeloid leukemia. *Blood* **107**, 3481-3485,
1097 doi:10.1182/blood-2005-09-3724 (2006).
- 1098 3 Bhansali, R. S., Pratz, K. W. & Lai, C. Recent advances in targeted therapies in acute myeloid
1099 leukemia. *Journal of hematology & oncology* **16**, 29, doi:10.1186/s13045-023-01424-6 (2023).
- 1100 4 DiNardo, C. D. *et al.* Venetoclax combined with decitabine or azacitidine in treatment-naïve,
1101 elderly patients with acute myeloid leukemia. *Blood* **133**, 7-17, doi:10.1182/blood-2018-08-
1102 868752 (2019).
- 1103 5 DiNardo, C. D. *et al.* Azacitidine and Venetoclax in Previously Untreated Acute Myeloid
1104 Leukemia. *The New England journal of medicine* **383**, 617-629, doi:10.1056/NEJMoa2012971
1105 (2020).
- 1106 6 Tsherniak, A. *et al.* Defining a Cancer Dependency Map. *Cell* **170**, 564-576 e516,
1107 doi:10.1016/j.cell.2017.06.010 (2017).
- 1108 7 Burger, J. A. Treatment of Chronic Lymphocytic Leukemia. *The New England journal of*
1109 *medicine* **383**, 460-473, doi:10.1056/NEJMra1908213 (2020).
- 1110 8 Jordan, V. C. & O'Malley, B. W. Selective estrogen-receptor modulators and antihormonal
1111 resistance in breast cancer. *Journal of clinical oncology : official journal of the American*
1112 *Society of Clinical Oncology* **25**, 5815-5824, doi:10.1200/JCO.2007.11.3886 (2007).
- 1113 9 Watson, P. A., Arora, V. K. & Sawyers, C. L. Emerging mechanisms of resistance to androgen
1114 receptor inhibitors in prostate cancer. *Nature reviews. Cancer* **15**, 701-711,
1115 doi:10.1038/nrc4016 (2015).
- 1116 10 Yu, A. L. *et al.* Anti-GD2 antibody with GM-CSF, interleukin-2, and isotretinoin for
1117 neuroblastoma. *The New England journal of medicine* **363**, 1324-1334,
1118 doi:10.1056/NEJMoa0911123 (2010).
- 1119 11 Burger, J. A. *et al.* Long-term efficacy and safety of first-line ibrutinib treatment for patients
1120 with CLL/SLL: 5 years of follow-up from the phase 3 RESONATE-2 study. *Leukemia* **34**, 787-
1121 798, doi:10.1038/s41375-019-0602-x (2020).
- 1122 12 Janku, F., Yap, T. A. & Meric-Bernstam, F. Targeting the PI3K pathway in cancer: are we
1123 making headway? *Nature reviews. Clinical oncology* **15**, 273-291,
1124 doi:10.1038/nrclinonc.2018.28 (2018).
- 1125 13 Millis, S. Z., Ikeda, S., Reddy, S., Gatalica, Z. & Kurzrock, R. Landscape of
1126 Phosphatidylinositol-3-Kinase Pathway Alterations Across 19 784 Diverse Solid Tumors.
1127 *JAMA oncology* **2**, 1565-1573, doi:10.1001/jamaoncol.2016.0891 (2016).
- 1128 14 Hirai, H. *et al.* MK-2206, an allosteric Akt inhibitor, enhances antitumor efficacy by standard
1129 chemotherapeutic agents or molecular targeted drugs in vitro and in vivo. *Molecular cancer*
1130 *therapeutics* **9**, 1956-1967, doi:10.1158/1535-7163.MCT-09-1012 (2010).

1131 15 Maira, S. M. *et al.* Identification and characterization of NVP-BKM120, an orally available pan-
1132 class I PI3-kinase inhibitor. *Molecular cancer therapeutics* **11**, 317-328, doi:10.1158/1535-
1133 7163.MCT-11-0474 (2012).

1134 16 Maira, S. M. *et al.* Identification and characterization of NVP-BEZ235, a new orally available
1135 dual phosphatidylinositol 3-kinase/mammalian target of rapamycin inhibitor with potent in vivo
1136 antitumor activity. *Molecular cancer therapeutics* **7**, 1851-1863, doi:10.1158/1535-7163.MCT-
1137 08-0017 (2008).

1138 17 Di Leo, A. *et al.* Buparlisib plus fulvestrant in postmenopausal women with hormone-receptor-
1139 positive, HER2-negative, advanced breast cancer progressing on or after mTOR inhibition
1140 (BELLE-3): a randomised, double-blind, placebo-controlled, phase 3 trial. *The Lancet.*
1141 *Oncology* **19**, 87-100, doi:10.1016/S1470-2045(17)30688-5 (2018).

1142 18 Hopkins, B. D. *et al.* Suppression of insulin feedback enhances the efficacy of PI3K inhibitors.
1143 *Nature* **560**, 499-503, doi:10.1038/s41586-018-0343-4 (2018).

1144 19 Krop, I. E. *et al.* Pictilisib for oestrogen receptor-positive, aromatase inhibitor-resistant,
1145 advanced or metastatic breast cancer (FERGI): a randomised, double-blind, placebo-
1146 controlled, phase 2 trial. *The Lancet. Oncology* **17**, 811-821, doi:10.1016/S1470-
1147 2045(16)00106-6 (2016).

1148 20 Furman, R. R. *et al.* Idelalisib and rituximab in relapsed chronic lymphocytic leukemia. *The*
1149 *New England journal of medicine* **370**, 997-1007, doi:10.1056/NEJMoa1315226 (2014).

1150 21 De Henau, O. *et al.* Overcoming resistance to checkpoint blockade therapy by targeting
1151 PI3Kgamma in myeloid cells. *Nature* **539**, 443-447, doi:10.1038/nature20554 (2016).

1152 22 Foubert, P., Kaneda, M. M. & Varner, J. A. PI3Kgamma Activates Integrin alpha(4) and
1153 Promotes Immune Suppressive Myeloid Cell Polarization during Tumor Progression. *Cancer*
1154 *immunology research* **5**, 957-968, doi:10.1158/2326-6066.CIR-17-0143 (2017).

1155 23 Schmid, M. C. *et al.* Receptor tyrosine kinases and TLR/IL1Rs unexpectedly activate myeloid
1156 cell PI3kgamma, a single convergent point promoting tumor inflammation and progression.
1157 *Cancer cell* **19**, 715-727, doi:10.1016/j.ccr.2011.04.016 (2011).

1158 24 Kaneda, M. M. *et al.* PI3Kgamma is a molecular switch that controls immune suppression.
1159 *Nature* **539**, 437-442, doi:10.1038/nature19834 (2016).

1160 25 Hong, D. S. *et al.* Eganelisib, a First-in-Class PI3Kgamma Inhibitor, in Patients with Advanced
1161 Solid Tumors: Results of the Phase 1/1b MARIO-1 Trial. *Clinical cancer research : an official*
1162 *journal of the American Association for Cancer Research* **29**, 2210-2219, doi:10.1158/1078-
1163 0432.CCR-22-3313 (2023).

1164 26 Gu, H. *et al.* PI3Kgamma maintains the self-renewal of acute myeloid leukemia stem cells by
1165 regulating the pentose phosphate pathway. *Blood*, doi:10.1182/blood.2023022202 (2024).

1166 27 Tyner, J. W. *et al.* Functional genomic landscape of acute myeloid leukaemia. *Nature* **562**,
1167 526-531, doi:10.1038/s41586-018-0623-z (2018).

1168 28 van Galen, P. *et al.* Single-Cell RNA-Seq Reveals AML Hierarchies Relevant to Disease
1169 Progression and Immunity. *Cell* **176**, 1265-1281 e1224, doi:10.1016/j.cell.2019.01.031
1170 (2019).

1171 29 Ng, S. W. *et al.* A 17-gene stemness score for rapid determination of risk in acute leukaemia.
1172 *Nature* **540**, 433-437, doi:10.1038/nature20598 (2016).

1173 30 Brinkman, E. K., Chen, T., Amendola, M. & van Steensel, B. Easy quantitative assessment of
1174 genome editing by sequence trace decomposition. *Nucleic acids research* **42**, e168,
1175 doi:10.1093/nar/gku936 (2014).

1176 31 Cancer Genome Atlas Research, N. *et al.* Genomic and epigenomic landscapes of adult de
1177 novo acute myeloid leukemia. *The New England journal of medicine* **368**, 2059-2074,
1178 doi:10.1056/NEJMoa1301689 (2013).

1179 32 Shymanets, A. *et al.* p87 and p101 subunits are distinct regulators determining class IB
1180 phosphoinositide 3-kinase (PI3K) specificity. *The Journal of biological chemistry* **288**, 31059-
1181 31068, doi:10.1074/jbc.M113.508234 (2013).

1182 33 Stephens, L. R. *et al.* The G beta gamma sensitivity of a PI3K is dependent upon a tightly
1183 associated adaptor, p101. *Cell* **89**, 105-114, doi:10.1016/s0092-8674(00)80187-7 (1997).

1184 34 Horejsi, Z. *et al.* CK2 phospho-dependent binding of R2TP complex to TEL2 is essential for
1185 mTOR and SMG1 stability. *Molecular cell* **39**, 839-850, doi:10.1016/j.molcel.2010.08.037
1186 (2010).

1187 35 Sarbassov, D. D., Guertin, D. A., Ali, S. M. & Sabatini, D. M. Phosphorylation and regulation
1188 of Akt/PKB by the rictor-mTOR complex. *Science* **307**, 1098-1101,
1189 doi:10.1126/science.1106148 (2005).

1190 36 Cantley, L. C. The phosphoinositide 3-kinase pathway. *Science* **296**, 1655-1657,
1191 doi:10.1126/science.296.5573.1655 (2002).

1192 37 Pham, L. V. *et al.* Strategic Therapeutic Targeting to Overcome Venetoclax Resistance in
1193 Aggressive B-cell Lymphomas. *Clinical cancer research : an official journal of the American*
1194 *Association for Cancer Research* **24**, 3967-3980, doi:10.1158/1078-0432.CCR-17-3004
1195 (2018).

1196 38 Sathe, A. *et al.* Parallel PI3K, AKT and mTOR inhibition is required to control feedback loops
1197 that limit tumor therapy. *PloS one* **13**, e0190854, doi:10.1371/journal.pone.0190854 (2018).

1198 39 Tavor, S. *et al.* CXCR4 regulates migration and development of human acute myelogenous
1199 leukemia stem cells in transplanted NOD/SCID mice. *Cancer research* **64**, 2817-2824,
1200 doi:10.1158/0008-5472.can-03-3693 (2004).

1201 40 Fields, T. A. & Casey, P. J. Signalling functions and biochemical properties of pertussis toxin-
1202 resistant G-proteins. *The Biochemical journal* **321** (Pt 3), 561-571, doi:10.1042/bj3210561
1203 (1997).

1204 41 Houslay, D. M. *et al.* Coincident signals from GPCRs and receptor tyrosine kinases are
1205 uniquely transduced by PI3Kbeta in myeloid cells. *Science signaling* **9**, ra82,
1206 doi:10.1126/scisignal.aae0453 (2016).

1207 42 Bondeson, D. P. *et al.* Lessons in PROTAC Design from Selective Degradation with a
1208 Promiscuous Warhead. *Cell chemical biology* **25**, 78-87 e75,
1209 doi:10.1016/j.chembiol.2017.09.010 (2018).

1210 43 Buhimschi, A. D. *et al.* Targeting the C481S Ibrutinib-Resistance Mutation in Bruton's Tyrosine
1211 Kinase Using PROTAC-Mediated Degradation. *Biochemistry* **57**, 3564-3575,
1212 doi:10.1021/acs.biochem.8b00391 (2018).

1213 44 Douglass, E. F., Jr., Miller, C. J., Sparer, G., Shapiro, H. & Spiegel, D. A. A comprehensive
1214 mathematical model for three-body binding equilibria. *Journal of the American Chemical*
1215 *Society* **135**, 6092-6099, doi:10.1021/ja311795d (2013).

1216 45 Wurz, R. P. *et al.* Affinity and cooperativity modulate ternary complex formation to drive
1217 targeted protein degradation. *Nature communications* **14**, 4177, doi:10.1038/s41467-023-
1218 39904-5 (2023).

1219 46 Lu, J. *et al.* Hijacking the E3 Ubiquitin Ligase Cereblon to Efficiently Target BRD4. *Chemistry*
1220 *& biology* **22**, 755-763, doi:10.1016/j.chembiol.2015.05.009 (2015).

1221 47 Garraway, L. A. *et al.* Integrative genomic analyses identify MITF as a lineage survival
1222 oncogene amplified in malignant melanoma. *Nature* **436**, 117-122, doi:10.1038/nature03664
1223 (2005).

1224 48 Chua, C. C. *et al.* Chemotherapy and Venetoclax in Elderly Acute Myeloid Leukemia Trial
1225 (CAVEAT): A Phase Ib Dose-Escalation Study of Venetoclax Combined With Modified
1226 Intensive Chemotherapy. *Journal of clinical oncology : official journal of the American Society*
1227 *of Clinical Oncology* **38**, 3506-3517, doi:10.1200/JCO.20.00572 (2020).

1228 49 Rahmani, M. *et al.* Cotargeting BCL-2 and PI3K Induces BAX-Dependent Mitochondrial
1229 Apoptosis in AML Cells. *Cancer research* **78**, 3075-3086, doi:10.1158/0008-5472.CAN-17-
1230 3024 (2018).

1231 50 Lin, K. H. *et al.* Targeting MCL-1/BCL-XL Forestalls the Acquisition of Resistance to ABT-199
1232 in Acute Myeloid Leukemia. *Scientific reports* **6**, 27696, doi:10.1038/srep27696 (2016).

1233 51 Evans, C. A. *et al.* Discovery of a Selective Phosphoinositide-3-Kinase (PI3K)-gamma
1234 Inhibitor (IPI-549) as an Immuno-Oncology Clinical Candidate. *ACS medicinal chemistry*
1235 *letters* **7**, 862-867, doi:10.1021/acsmedchemlett.6b00238 (2016).

1236 52 Gangadhara, G. *et al.* A class of highly selective inhibitors bind to an active state of
1237 PI3Kgamma. *Nature chemical biology* **15**, 348-357, doi:10.1038/s41589-018-0215-0 (2019).

1238 53 Vanhaesebroeck, B., Ali, K., Bilancio, A., Geering, B. & Foukas, L. C. Signalling by PI3K
1239 isoforms: insights from gene-targeted mice. *Trends in biochemical sciences* **30**, 194-204,
1240 doi:10.1016/j.tibs.2005.02.008 (2005).

1241 54 Nurnberg, B. & Beer-Hammer, S. Function, Regulation and Biological Roles of PI3Kgamma
1242 Variants. *Biomolecules* **9**, doi:10.3390/biom9090427 (2019).

1243 55 Perino, A., Ghigo, A., Scott, J. D. & Hirsch, E. Anchoring proteins as regulators of signaling
1244 pathways. *Circulation research* **111**, 482-492, doi:10.1161/CIRCRESAHA.111.262899
1245 (2012).

1246 56 Patrucco, E. *et al.* PI3Kgamma modulates the cardiac response to chronic pressure overload
1247 by distinct kinase-dependent and -independent effects. *Cell* **118**, 375-387,
1248 doi:10.1016/j.cell.2004.07.017 (2004).

1249 57 Beretta, M., Bauer, M. & Hirsch, E. PI3K signaling in the pathogenesis of obesity: The cause
1250 and the cure. *Advances in biological regulation* **58**, 1-15, doi:10.1016/j.jbior.2014.11.004
1251 (2015).

1252 58 Damilano, F., Perino, A. & Hirsch, E. PI3K kinase and scaffold functions in heart. *Annals of*
1253 *the New York Academy of Sciences* **1188**, 39-45, doi:10.1111/j.1749-6632.2009.05081.x
1254 (2010).

1255 59 Mohan, M. L. & Naga Prasad, S. V. Scaffolding Function of PI3Kgamma Emerges from
1256 Enzyme's Shadow. *Journal of molecular biology* **429**, 763-772, doi:10.1016/j.jmb.2017.01.023
1257 (2017).

1258 60 Winter, G. E. *et al.* DRUG DEVELOPMENT. Phthalimide conjugation as a strategy for in vivo
1259 target protein degradation. *Science* **348**, 1376-1381, doi:10.1126/science.aab1433 (2015).

1260 61 Bai, L. *et al.* A Potent and Selective Small-Molecule Degradator of STAT3 Achieves Complete
1261 Tumor Regression In Vivo. *Cancer cell* **36**, 498-511 e417, doi:10.1016/j.ccell.2019.10.002
1262 (2019).

1263 62 Kaneshige, A. *et al.* A selective small-molecule STAT5 PROTAC degrader capable of
1264 achieving tumor regression in vivo. *Nature chemical biology* **19**, 703-711,
1265 doi:10.1038/s41589-022-01248-4 (2023).

1266 63 Koide, E. *et al.* Development and Characterization of Selective FAK Inhibitors and PROTACs
1267 with In Vivo Activity. *Chembiochem : a European journal of chemical biology* **24**, e202300141,
1268 doi:10.1002/cbic.202300141 (2023).

1269 64 Langmead, B., Trapnell, C., Pop, M. & Salzberg, S. L. Ultrafast and memory-efficient
1270 alignment of short DNA sequences to the human genome. *Genome biology* **10**, R25,
1271 doi:10.1186/gb-2009-10-3-r25 (2009).

1272 65 Ramirez, F. *et al.* deepTools2: a next generation web server for deep-sequencing data
1273 analysis. *Nucleic acids research* **44**, W160-165, doi:10.1093/nar/gkw257 (2016).

1274 66 Pohl, A. & Beato, M. bwtool: a tool for bigWig files. *Bioinformatics* **30**, 1618-1619,
1275 doi:10.1093/bioinformatics/btu056 (2014).

1276 67 Martz, C. A. *et al.* Systematic identification of signaling pathways with potential to confer
1277 anticancer drug resistance. *Science signaling* **7**, ra121, doi:10.1126/scisignal.aaa1877
1278 (2014).

1279 68 Su, A. *et al.* The Folate Cycle Enzyme MTHFR Is a Critical Regulator of Cell Response to
1280 MYC-Targeting Therapies. *Cancer discovery* **10**, 1894-1911, doi:10.1158/2159-8290.CD-19-
1281 0970 (2020).

1282 69 Lin, K. H. *et al.* P2RY2-AKT activation is a therapeutically actionable consequence of XPO1
1283 inhibition in acute myeloid leukemia. *Nature cancer* **3**, 837-851, doi:10.1038/s43018-022-
1284 00394-x (2022).

1285 70 Kuo, Y. H. *et al.* Cbf beta-SMMHC induces distinct abnormal myeloid progenitors able to
1286 develop acute myeloid leukemia. *Cancer cell* **9**, 57-68, doi:10.1016/j.ccr.2005.12.014 (2006).

- 1287 71 Pimentel, H., Bray, N. L., Puente, S., Melsted, P. & Pachter, L. Differential analysis of RNA-
1288 seq incorporating quantification uncertainty. *Nature methods* **14**, 687-690,
1289 doi:10.1038/nmeth.4324 (2017).
- 1290 72 Hanzelmann, S., Castelo, R. & Guinney, J. GSEA: gene set variation analysis for microarray
1291 and RNA-seq data. *BMC bioinformatics* **14**, 7, doi:10.1186/1471-2105-14-7 (2013).
- 1292 73 Trott, O. & Olson, A. J. AutoDock Vina: improving the speed and accuracy of docking with a
1293 new scoring function, efficient optimization, and multithreading. *Journal of computational*
1294 *chemistry* **31**, 455-461, doi:10.1002/jcc.21334 (2010).

FIGURE LEGENDS

1295 **Figure 1: AML Cells Exhibit a Selective Dependency on PIK3CG and its Regulatory Subunit**
1296 **PIK3R5.**

1297 **A.** Expression of catalytic and regulatory Class I PI3K isoforms in normal and tumor tissue
1298 samples. Primary tumor expression data from TCGA database; normal expression data from
1299 GeTex expression database. Data accessed through Gepia gene expression portal.

1300 **B.** Heatmap of normalized read density of H3K27ac ChIP-seq of 66 AML patient samples and
1301 four CD34⁺ healthy donors' samples. Bar graphs represent the sum of depicted region signal for
1302 each sample.

1303 **C.** DepMap CRISPR/Cas9 dependency profiling data depicting essentiality of the four catalytic
1304 and regulatory isoforms of PI3K. Data are ordered by unsupervised hierarchical clustering of Min-
1305 Max normalized averaged dependencies across cell lines in a given cancer type. Only cancer
1306 types with > 5 cell lines were included in analysis.

1307 **D.** Cell growth of OCI-AML2 cells following shRNA-mediated depletion of *PIK3CA*, *PIK3CB*,
1308 *PIK3CD*, or *PIK3CG*. Data were normalized to values obtained from the corresponding –
1309 doxycycline condition. Error bars represent mean \pm SD of three biological replicates after three
1310 days of seeding. P-values calculated using Welch *t* test.

1311 **E.** PIK3CG levels by western blot in OCI-AML2 cells transduced with a non-targeting control and
1312 two *PIK3CG*-directed sgRNAs. ACTIN used as a loading control.

1313 **F.** Cell growth over time of indicated AML cell lines transduced with either a non-targeting control
1314 or two *PIK3CG*-directed sgRNAs. Error bars represent mean \pm SD of seven technical replicates
1315 in three biological repeats.

G. PIK3R5 levels by western blot in OCI-AML2 cells transduced with a non-targeting control and two *PIK3R5*-directed sgRNAs. ACTIN used as a loading control.

H. Cell growth over time of indicated AML cell lines transduced with either a non-targeting control or two *PIK3CG*-directed sgRNAs. Error bars represent mean \pm SD of seven technical replicates in three biological repeats.

I. Colony formation from indicated AML cell lines infected with either a control, or two sgRNAs directed against *PIK3CG* or *PIK3R5*. Error bars represent mean \pm SD of five technical replicates in three biological repeats.

J. Bioluminescence signal detected by *in vivo* IVIS imaging of OCI-AML2 cells infected with a control or a *PIK3CG*-directed sgRNA and injected into NSG mice (n=10 mice / group) across multiple time points (days 7, 13, 18, 22). Error bars represent mean \pm SD. P-values calculated using two-way ANOVA.

F, H, and I. P-values calculated using one-way ANOVA.

Figure 2: *PIK3CG* and *PIK3R5* Suppression Potentiates the Anti-Leukemia Effect of Venetolax.

A. Spearman correlation between *PIK3CG* and *PIK3R5* expression and AUC responses to small-molecules screened as part of the BEAT-AML project²⁷.

B. Venetoclax sensitivity in patients from the BEAT-AML cohort who are part, or not part, of the FAB4 and 5 subgroups. Error bars represent mean \pm SD. P-values calculated using a Wilcoxon test.

C. Cell sensitivity represented as half-maximal inhibitory concentration (IC₅₀s, top) and Area Under the Curves (AUCs, bottom) of OCI-AML2 cells transduced with either a non-targeting

control, two *PIK3CG*-directed, or two *PIK3R5*-directed sgRNAs and treated with increasing concentrations of the indicated targeted therapies or chemotherapy drugs. Error bars represent mean \pm SD of four technical replicates after three days of seeding in two biological repeats.

D. Venetoclax sensitization effect (representative dose response curves, left panel, and AUCs, right panel) of two *PIK3CG*- and *PIK3R5*-directed sgRNAs in MOLM-14 and OCI-AML3 cell lines treated with increasing doses of venetoclax. Error bars represent mean \pm SD of five technical replicates after three days of seeding in two biological repeats.

E. Colony formation from various AML cell lines infected with either a control, or two sgRNAs directed against *PIK3CG* or *PIK3R5*, and treated with 250nM, 5 μ M, or 150nM venetoclax in OCI-AML2, OCI-AML3, and MOLM-14, respectively. Error bars represent mean \pm SD of four technical replicates after seven days of seeding in three biological repeats.

F. PIK3CA, PIK3CB and PIK3CD levels by western blot in OCI-AML2 cells transduced with a non-targeting control and two *PIK3CG*-directed sgRNAs. ACTIN used as a loading control.

G. Representative growth inhibition curve (left panel) and AUCs (right panel) of OCI-AML2 cells infected with a non-targeting control and a *PIK3CA*-, *PIK3CB*-, or *PIK3CD*-directed sgRNA and treated with increasing venetoclax. Error bars represent mean \pm SD of seven technical replicates after three days of seeding in three biological repeats.

C-E, G. P-values calculated using one-way ANOVA.

H. Proportion of GFP-positive OCI-AML2 cells infected with a control or a *PIK3CG*-directed sgRNA and injected in NSG mice treated with either vehicle or 100mg/kg venetoclax (n=8 mice / group). Error bars represent mean \pm SD. P-values calculated using Mann-Whitney.

I. Bioluminescence signal detected over multiple indicated time points of OCI-AML2 cells infected with a control or a *PIK3CG*-directed sgRNA and injected into NSG mice (n=8 mice / group) and

1362 treated with either vehicle or 100mg/kg venetoclax. Error bars represent mean \pm SD. P-values
1363 calculated using two-way ANOVA.

1364 **J.** Overall survival of mice transplanted with either OCI-AML2 cells infected with a non-targeting
1365 or a *PIK3CG*-direct sgRNA alone or in combination with 100 mg/kg venetoclax daily from day 25
1366 (n=10 mice/ group). Statistical significance by log-rank (Mantel-Cox) test.

1367
1368 **Figure 3: PIK3CG and PIK3R5 Selectively Control AKT Signaling in AML.**

1369 **A.** Network of the top PIK3R5-interacting proteins in at least two AML cell lines from a tandem
1370 affinity purification of PIK3R5/p101. Known physical interaction from StringDB (score > 0.5).

1371 **B.** Correlation between gene dependency scores of *AKT1* and *AKT2* versus *PIK3CG* in a panel
1372 of 15 AML cell lines. Data from DepMap CRISPR/Cas9 dependency profiling. Pearson correlation
1373 coefficient (ρ) and p-value provided to demonstrate correlation and significance.

1374 **C.** Top MK-2206 sensitizer and resistor candidate genes identified from a pooled drug-modifier
1375 screen conducted in OCI-AML2 cells. Gene-level scores were obtained by averaging sgRNA-
1376 level comparisons. Genes with a log₂ depletion of < - 0.5 or enrichment of > 0.5 designated in
1377 orange and blue dots, respectively. Red dot denotes *BCL2*. Non-targeting control genes depicted
1378 as grey dots.

1379 **D.** Expression and phosphorylation levels of PIK3CG, PIK3R5, AKT, and AKT substrates by
1380 western blot in OCI-AML2 and OCI-AML3 cells transduced with a non-targeting control, and one
1381 representative PIK3CG- and *PIK3R5*-directed sgRNA.

1382 **E.** AKT1 and AKT2 phosphorylation levels by western blot in OCI-AML2 cells following knockout
1383 of *PIK3CG* and *PIK3R5*.

F. Indicated pro- and anti-apoptotic protein levels by western blot following knockout of *PIK3CG* and *PIK3R5* using one representative sgRNA in OCI-AML2 cells.

G. Catalytic PI3K subunit levels and phosphorylation of AKT by western blot following knockdown of indicated catalytic PIK3 subunits in OCI-AML2 cells. ACTIN used as a loading control.

H. Fold-change in mRNA expression levels of each regulatory PI3K subunit following their knockdown. Error bars represent mean \pm SD of three biological replicates. P-values calculated using Welch *t* test.

I. AKT phosphorylation levels by western blot following knockdown of regulatory subunits of AKT in OCI-AML2 cells.

J. Phosphorylation levels of AKT and a downstream substrate, TSC2, by western blot following ectopic expression of wild-type *PIK3CG* in OCI-AML2 cells infected with an shRNA targeting the 3' UTR region of *PIK3CG*.

K. Schematic of the PI3K signaling downstream G-coupled protein receptors (GPCR) and tyrosine kinase receptors (RTK). CXCL12 activates GPCRs whereas pertussis toxin blocks their activity.

L. AKT and TSC2 phosphorylation levels by western blot in indicated human AML cell lines treated with 100ng/mL pertussis toxin Ptx for 24 hours.

M. Phosphorylation levels of AKT and its downstream substrate PRAS40 by western blot in control or *PIK3CG*-depleted OCI-AML2 cells treated with 200ng/mL SDF1 α in serum-free media for 30 minutes.

Figure 4: PROteolysis Targeting Chimera (PROTAC)-Based PIK3CG Degradation Is a Promising Strategy to Durably Suppress AKT Signaling in AML.

1406 **A-B.** Relative cell growth (**A**) and colony formation capacity (**B**) of OCI-AML2 cells following
1407 sgRNA-mediated suppression of *PIK3CG* or *PIK3R5*, or treated with indicated concentrations of
1408 small-molecule inhibitors of PIK3CG, IPI-549 and AZ2. Error bars represent mean \pm SD of seven
1409 replicates (A) in two biological repeats for the knockout experiment and three biological repeats
1410 for the pharmacological study, and four technical replicates (B) in three biological repeats.

1411 **C.** Growth inhibition, IC₅₀ and AUC values, of OCI-AML2 cells treated once, twice or thrice
1412 iteratively with increasing concentrations of IPI-549, or AZ2. Error bars represent mean \pm SD of
1413 seven technical replicates in two biological repeats.

1414 **D.** AKT phosphorylation levels by western blot in OCI-AML2 cells either infected with *PIK3CG*-
1415 and *PIK3R5*-directed sgRNAs for 72 hours or treated with 500nM IPI-549, AZ2, or the AKT
1416 inhibitor, MK-2206, for one and 72 hours.

1417 **E.** AKT phosphorylation levels by western blot of OCI-AML2 cells treated for one hour, 72 hours,
1418 or 72 hours followed by fresh addition of 500nM IPI-549, AZ2, or MK-2206 for one hour.

1419 **F.** Simulation of the docking of AZ2 in the PIK3CG pocket. The parental AZ2 inhibitor is shown to
1420 be converted to ARM165 degrader by capitalizing on the presence of the acetyl moiety, that is
1421 orientated towards the outside of the kinase pocket, to which a linker and subsequent CEREBLON
1422 recruiting moiety is attached to generate the PIK3CG degrader compound, ARM165.

1423 **G.** PIK3CG and PIK3R5 levels by western blot in OCI-AML2 cells treated with increasing
1424 concentrations of ARM165. ACTIN used as a loading control. Q: quantification of PIK3CG levels.

1425 **H.** PIK3CG expression level by western blot in OCI-AML2 cells treated with 1 μ M ARM165 in
1426 combination with either 10nM bortezomib or 10 μ M lenalidomide for 24 hours.

1427 **I.** PIK3CG expression level by western blot in HEK293T cells expressing either wild-type or a
1428 lysine to arginine mutant form of PIK3CG (K437R, K444R, K455R, K457R, K490R, K510R,
1429 K531R, K553R, K572R, K584R, K587R, and K597R). ACTIN used as a loading control.

1430 **J.** Colony formation from OCI-AML2 cells harboring either a control or a *PIK3CG*-directed sgRNA
1431 and treated with 600nM ARM165. Error bars represent mean \pm SD of four and five technical
1432 replicates after seven days of seeding in two biological repeats.

1433 **K.** Proportion of mTagBFP-positive OCI-AML2 cells infected with a control (sgCT), and two
1434 CRBN-directed sgRNAs (sgCRBN_1 and sgCRBN_2) and treated with 3 μ M ARM165. Error bars
1435 represent mean \pm SD of three biological replicates after three days of seeding. P-values calculated
1436 using Welch *t* test.

1437 **L.** Quantitative proteomics analysis of PIK3CG-expressing HEK293T cells treated with 2 μ M
1438 ARM165 for 24 hours. Volcano plot threshold applied at p-value $\leq 10^{-4}$ and absolute log₂ (FC) \geq
1439 0.8.

1440 **M.** Phosphorylation levels of AKT and its substrate PRAS40 by western blot in OCI-AML2 cells
1441 infected with a control, a representative *PIK3CG*-, or *PIK3R5*-directed sgRNA or treated with 1 μ M
1442 ARM165 for 72 hours.

1443 **N.** Representative growth inhibition curves (left panel), IC₅₀s, and AUCs (right panel) in response
1444 to increasing concentrations of ARM165 of OCI-AML2 cells infected with either a control or a
1445 myristoylated form of AKT. Error bars represent mean \pm SD of seven technical replicates after
1446 three days of seeding in three biological repeats. P-values calculated using Mann Whitney.

1447 **A, B, J, K.** P-values calculated using one-way ANOVA.

1448

Figure 5: Degradation of PIK3CG Demonstrated Superior Cytotoxic Performance Relative to Existing Small-Molecule Inhibitors of PIK3CG.

A. Representative growth inhibition curves, IC₅₀ and AUC values, of two human AML cell lines treated with increasing doses of ARM204 (a non-PIK3CG targeting inactive small-molecule analog to ARM165), AZ2, and ARM165. Error bars represent the mean \pm SD of seven technical replicates after three days of seeding.

B. AUCs reflecting viability of multiple indicated human AML and non-AML cell lines treated with increasing ARM204, AZ2, and ARM165. Error bars represent mean \pm SD of seven technical replicates after three days of seeding in three biological repeats. P-values calculated using one-way ANOVA.

C. Growth inhibition, IC₅₀ and AUC values, of four primary samples from patients with AML treated with increasing AZ2 and ARM165. Error bars represent mean \pm SD of four technical replicates after five days of seeding.

D. Principal component analysis of OCI-AML2 and MOLM-14 cells treated with DMSO, 1 μ M and 500nM AZ2 or ARM-165 for 24 hours, respectively.

E. Representative upregulated and downregulated pathways along with their respective biological functions, using the top dysregulated genes (with q-values < 0.001) common to ARM165-treated OCI-AML2 and MOLM-14 cells.

F. Heatmaps of leading-edge genes of biological pathways reported in panel E and their expression levels compared to DMSO following AZ2 and ARM165 treatments of MOLM-14 cells.

G. Proportion of Annexin V-positive MOLM-14 and OCI-AML2 cells treated with 500nM and 1 μ M ARM165, respectively, for 48 hours. Error bars represent mean \pm SD of three biological replicates. P-values calculated using Welch *t* test.

H. ARM165 gene signature representation in AML patients from the BEAT-AML cohort with low versus high *PIK3CG* expression. ON versus OFF ARM165 signatures were assigned for each patient based on their ES score below or above the median, respectively. The number of ARM165-ON patients in the *PIK3CG* high subset versus the *PIK3CG* low subset was compared. P-values using Fisher's t-test.

Figure 6. *PIK3CG* Degradation Potentiates the Effect of Venetoclax in Multiple AML Models.

A. Venetoclax sensitization effect of AZ2, or ARM165 across indicated human AML cell lines. Error bars represent mean \pm SD of seven technical replicates after three days of seeding in three biological repeats.

B. Colony formation from five human AML cell lines treated with AZ2 or ARM165 in combination with venetoclax (MOLM-14: 0.75 μ M AZ2 or ARM165, and 375nM venetoclax; MV4-11: 0.5 μ M AZ2 or ARM, and 75nM venetoclax; OCI-AML2: 1 μ M AZ2 or ARM165, and 500nM venetoclax; NOMO-1: 0.625 μ M ARM165 or AZ2, and 10 μ M venetoclax; HL60: 1 μ M ARM or AZ2, and 2.5 μ M venetoclax). Error bars represent mean \pm SD of four technical replicates after seven days of seeding in three biological repeats.

C. Growth inhibition curves (left panel), IC50 values, and AUCs (right panel) of OCI-AML2 cells treated with DMSO or 500nM ARM165 in combination with increasing doses of either venetoclax, an MCL1 inhibitor, S63845, or two BCL-XL inhibitors, WEHI-539 and A-1331852. Error bars represent mean \pm SD of seven technical replicates after three days of seeding in three biological repeats.

D. Colony formation from two human AML primary samples treated with indicated AZ2 or ARM165 concentrations in combination with 375nM venetoclax. Error bars represent mean \pm SD of four technical replicates after seven days of seeding.

1496 **A-D.** P-values calculated using one-way ANOVA.

1497 **E.** Bliss synergy plots for two primary patient samples with AML and treated with ARM165 and
1498 venetoclax across a drug-dilution matrix for five days. Delta scores from high synergy (lighter
1499 blue) to no synergy (dark blue).

1500 **F.** Bliss synergy scores for 9 primary patient samples with AML and treated with a drug-dilution
1501 matrix of AZ2 and venetoclax, or ARM165 and venetoclax. Bars represent median and violin plots
1502 represent range. P-values calculated using Mann-Whitney test.

1503 **G.** *In vivo* limiting dilution assay performed with primary murine *Cbfb-MYH11* leukemic cells
1504 treated for 24h with 0.5 μ M AZ2 or ARM165 and injected into sublethally-irradiated recipient
1505 animals at decreasing cell concentrations. Determination of Leukemia-Initiating Cell (LIC)
1506 frequency with a 95% confidence interval in each group using Extreme Limiting Dilution Analysis
1507 (ELDA). Two-sided chi-squared test used for statistics.

1508 **H.** Proportion of *Cbfb-MYH11*-driven GFP-positive leukemic blasts in bone marrow of euthanized
1509 animals treated by intravenous injection with vehicle (Veh), 0.051mg/kg AZ2, or 0.051mg/kg
1510 ARM165 for five consecutive days (n=9 mice per group). Error bars represent mean \pm SD.

1511 **I.** Proportion of *Cbfb-MYH11*-driven GFP-positive leukemic blasts in spleen (left panel) and
1512 corresponding spleen weight (right panel) of euthanized animals treated by intravenous injection
1513 with vehicle (Veh) or 0.051mg/kg ARM165 for five consecutive days (n=11 mice in vehicle and
1514 n=10 mice in ARM165 group). Error bars represent mean \pm SD.

1515 **J. Left panel** Proportion of blood circulating *Cbfb-MYH11*-driven GFP-positive blasts in animals
1516 treated by intravenous injection with vehicle (Veh), 0.051mg/kg AZ2, or 0.051mg/kg ARM165 in
1517 combination with 100mg/kg venetoclax for five consecutive days (n=5 mice per group). Error bars
1518 represent mean \pm SD. **Right panel.** Proportion of blood circulating CD45-positive human AML
1519 primary blasts in animals transplanted with a PDX for a month and then treated by intravenous

1520 injection with vehicle (Veh) or 0.051mg/kg ARM165 in combination with 100mg/kg venetoclax for
1521 consecutive days (n=5 mice per group). Error bars represent mean \pm SD.
1522 **H-J.** P-values calculated using Mann-Whitney test.

LEGENDS TO SUPPLEMENTARY FIGURES AND TABLES

Figure S1: A. Comparison of the expression levels of *PIK3CG* and *PIK3R5* across AML and healthy tissues. P-values calculated using one-way ANOVA. **B-D.** Expression levels of *PIK3CG* and *PIK3R5* in AML patients from various FAB (**B**) and genetic (**C**) subcategories, or at diagnosis versus relapse (**D**). P-values calculated using Wilcoxon test. **E and F.** Spearman correlation between AML cell differentiation state and the expression of *PIK3CG* and *PIK3R5*. **B-F.** Data generated using the BEAT-AML cohort.

Figure S2: A. DNA sanger sequencing of the *PIK3CG* and *PIK3R5* genomic regions targeted by the CRISPR-Cas9 *PIK3CG*- and *PIK3R5*-directed guides in OCI-AML2 cells. Sequences were aligned using TIDE online tool to determine the relative efficiency of each sgRNA. **B.** Bioluminescence pictures of three representative mice from Figure 1J injected with OCI-AML2 infected with either a non-targeting control or a *PIK3CG*-directed sgRNA. Median bioluminescence is depicted in radiance on days 7, 13, 18 and 22.

Figure S3: A and B. Representative growth inhibition curves, and corresponding IC50 and AUC values from Figure 2C of OCI-AML2 cells transduced with either a non-targeting control, two *PIK3CG*-directed, or two *PIK3R5*-directed sgRNAs and treated with increasing concentrations of the indicated targeted therapies or chemotherapy drugs (**A**), FLT3 inhibitors, gilteritinib and sorafenib, or KIT inhibitors, amuvanib and telatinib (**B**). Error bars represent mean \pm SD of four (A) and seven (B) replicates after three days of seeding. Av. = Averaged. **C.** Bioluminescence pictures of three representative mice from Figure 2I injected with OCI-AML2 cells harboring a non-targeting control or *PIK3CG*-directed sgRNA. Median bioluminescence is depicted in radiance on days 17, 24, 27 and 31.

Figure S4: A. Volcano plots of the PIK3R5-interacting protein pulled down in OCI-AML2, MV4-11, and NOMO-1 cells compared to control. **B.** Ranking of proteins with positive infinite ratios (only identified in PIK3R5 pull down) according to the number of peptides identified. Only proteins with a z-test score > 0.95 were included for further analysis. **C.** Network corresponding to Figure 3A depicting, in two colors, the PIK3R5-interacting proteins identified in two cell lines (in yellow) or all three cell lines (in orange).

Figure S5: A. Correlation between gene dependency scores of *AKT1* and *AKT2* versus *PIK3CG* in a panel of non-AML cell lines. Data from DepMap CRISPR/Cas9 dependency profiling. Pearson correlation coefficient (ρ) provided to demonstrate no correlation. **B.** MK-2206 sensitizer and resistor topoisomerase-encoding genes, polymerase-encoding genes, and anti-apoptotic protein-encoding genes identified from a pooled drug-modifier screen conducted in OCI-AML2 cells. Gene-level scores were obtained by averaging sgRNA-level comparisons. Red dot denotes *BCL2* identified as a sensitizer gene. All other genes included in the analysis are depicted as blue dots. **C.** Chemokine/receptor expression heatmap indicating upregulation of both CXCL12/CXCR4 in AML relative to normal tissue. Tumor expression data from TCGA database; normal expression data from GeTex expression database. Data accessed through Gepia gene expression portal.

Figure S6: Synthetic scheme for the synthesis of the PIK3CG degrader, ARM165. Reagents and conditions: i) LiOH monohydrate, MeOH, H₂O, 60°C, 40 h (94%) ; ii) Boc-AOc-OH, T3P 50% in ethyl acetate, pyridine, *N,N*-dimethylformamide, 80°C, 16 h ; iii) TFA, CH₂Cl₂, r.t. 2 h ; iv) Glutaric anhydride, *N,N*-diisopropylethylamine, toluene, *N,N*-dimethylformamide, 110°C, 2 h (62% over 3 steps, ii-iv) ; v) Compound I, HATU, *N,N*-diisopropylethylamine, *N,N*-dimethylformamide, r.t. 16 h (55%).

Figure S7: A. Representative growth inhibition curves, with IC50s and AUCs, corresponding to the Figure 5B for AML and non-AML cells treated with increasing doses of ARM204, AZ2, and ARM165. Error bars represent mean \pm SD of seven replicates after three days of seeding. **B.** Synthetic scheme for the synthesis of non-PIK3CG-targeting control compound for ARM165, ARM204. Reagents and conditions are provided below the synthesis scheme.

Figure S8: A. Representative growth inhibition curves, IC50s, and AUC values, corresponding to Figure 6A of indicated AML cells treated with increasing doses of venetoclax in presence of AZ2 or ARM165. Error bars represent mean \pm SD of seven replicates after three days of seeding. **B-C.** Growth inhibition curves, IC50s, and AUC values of OCI-AML2 cells treated with increasing doses of cytarabine, daunorubicin, or venetoclax in combination with 500nM ARM165. Error bars represent mean \pm SD of seven technical replicates after three days of seeding in three biological repeats. P-values calculated using one-way ANOVA.

Figure S9: A-B. Toxicity profile of ARM165 treatment in naive mice. Mice were treated with IV injection of 0.051mg/kg ARM165 for seven consecutive days. Individual mouse weight was measured daily (n=5 mice per group) (**A**) and the proportion of each indicated hematopoietic cell fraction (**B**) was established in blood using an MS9 instrument, and in bone marrow (BM) and spleen (SP) by flow cytometry (n=10 mice per group). Error bars represent mean \pm SD. P-values calculated using Mann-Whitney.

Figure S10: Flow cytometry gating strategy for assessment of the Proportion of GFP-positive *Cbfb-MYH11* leukemic blasts.

Figure S11: Flow cytometry gating strategy for assessment of the proportion of hCD45-positive human leukemic blasts.

Figure S12: Flow cytometry gating strategy for assessment of the proportion of mTagBFP-positive OCI-AML2 cells.

Table S1: List of abbreviations related to tissue-specific cancers used for expression analysis in Figure 1A.

Table S2: Candidate proteins which interact with PIK3R5 in at least two out of the three profiled AML cell lines.

Table S3: Proteomic-based selectivity profile of ARM165.

Table S4: Clinical annotations of the 9 primary samples of patients with AML used in the study. Female = 0, Male = 1.

Table S5: ARM165 transcriptional gene signature used for the ssGSEA analysis.

Figure 1

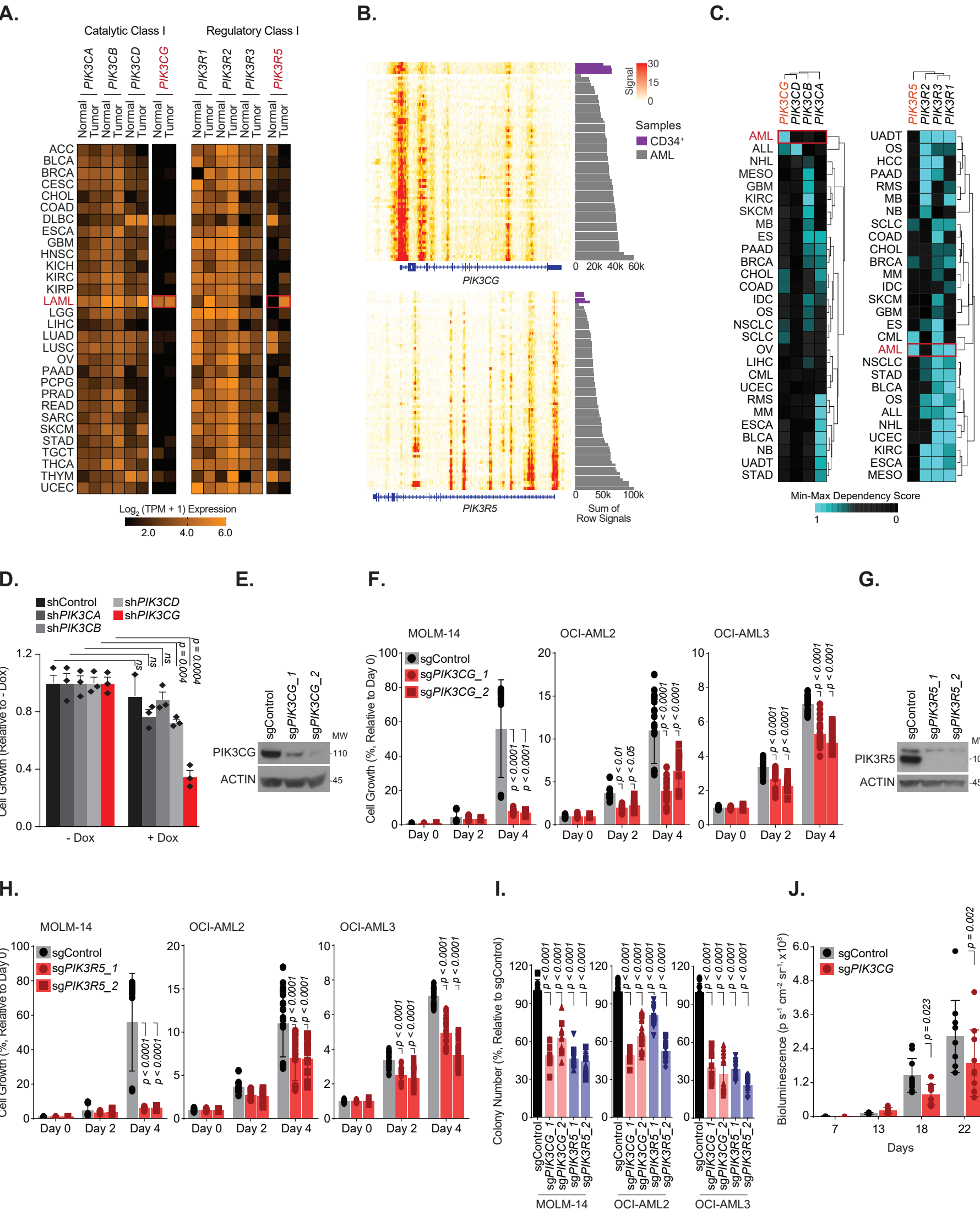


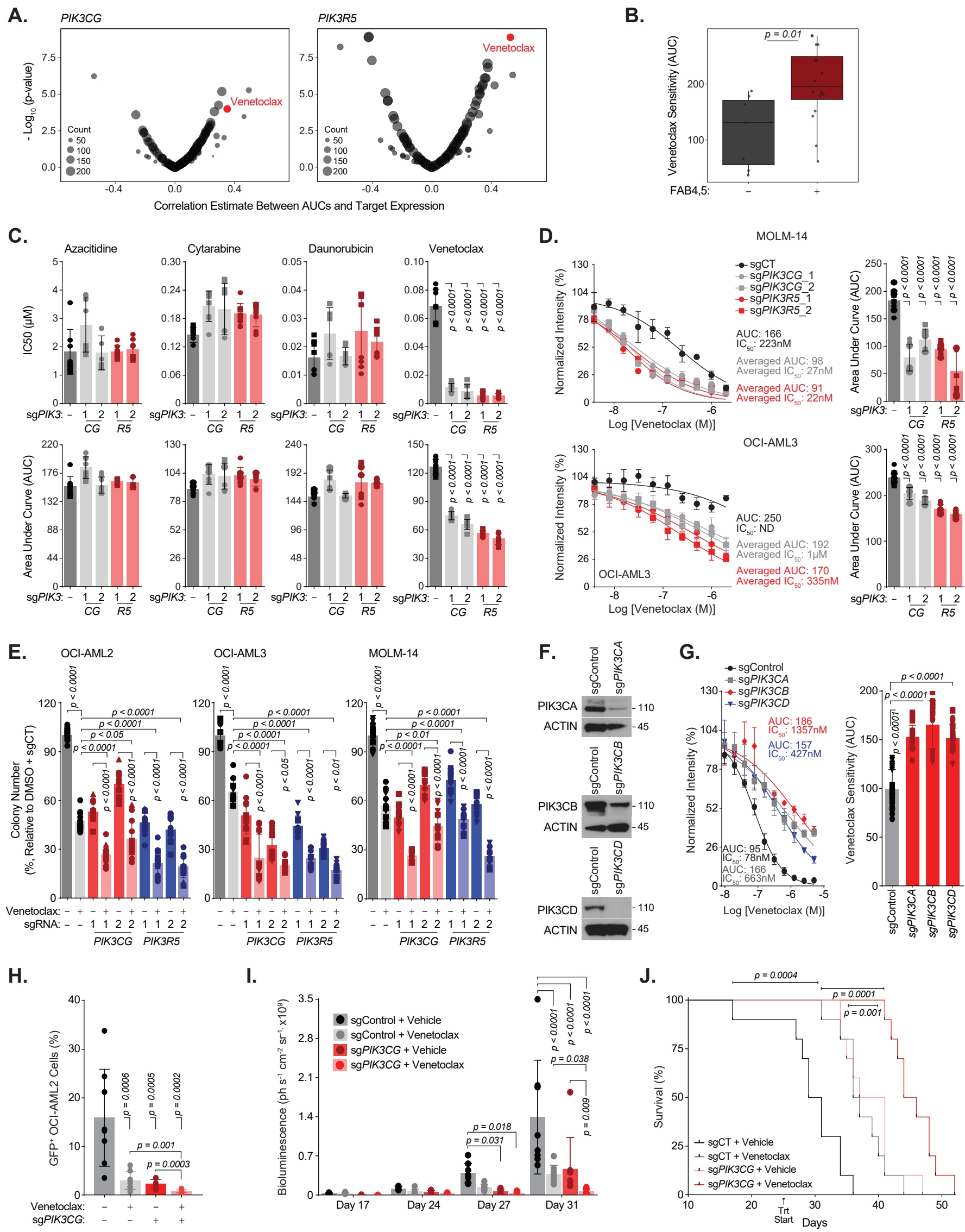
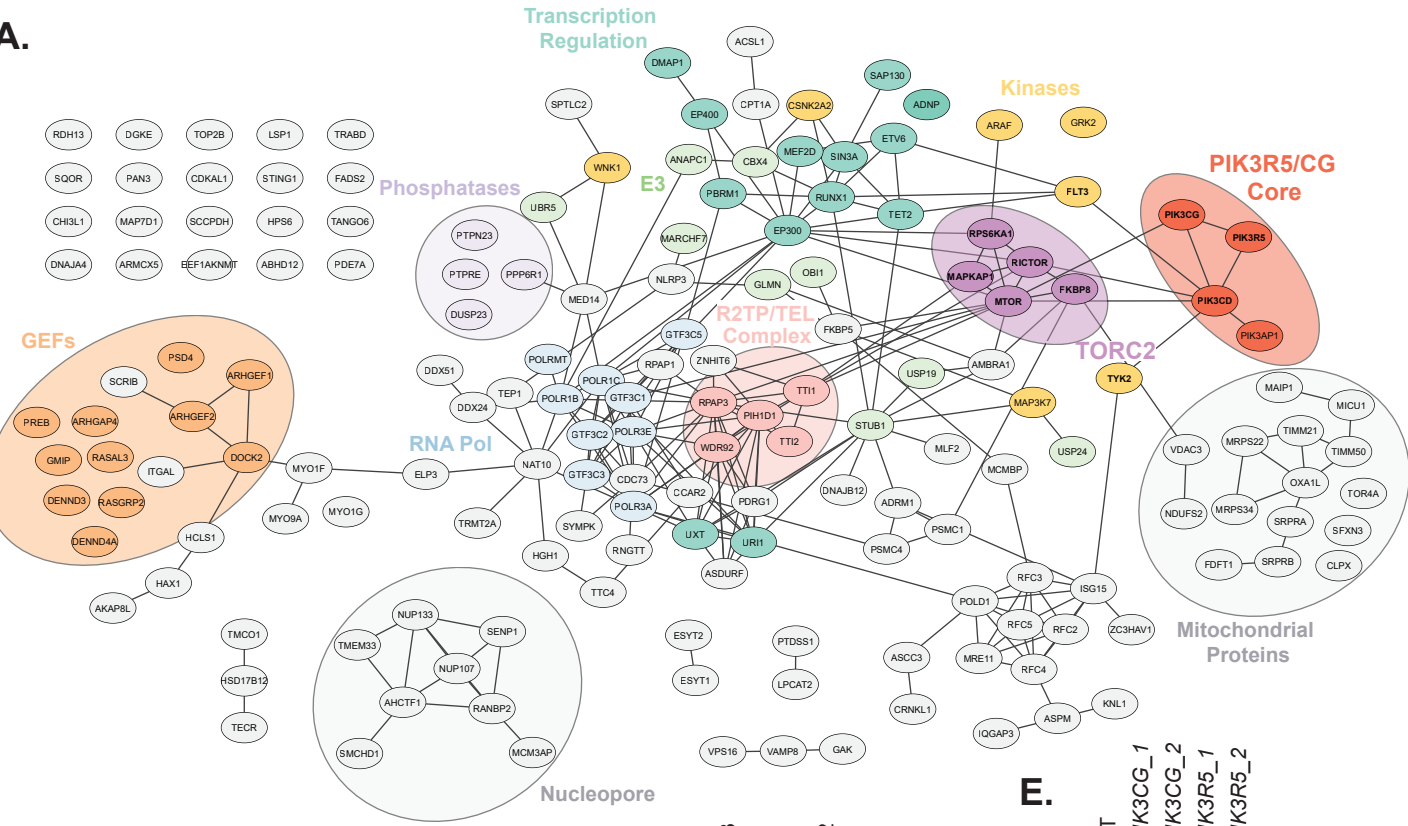
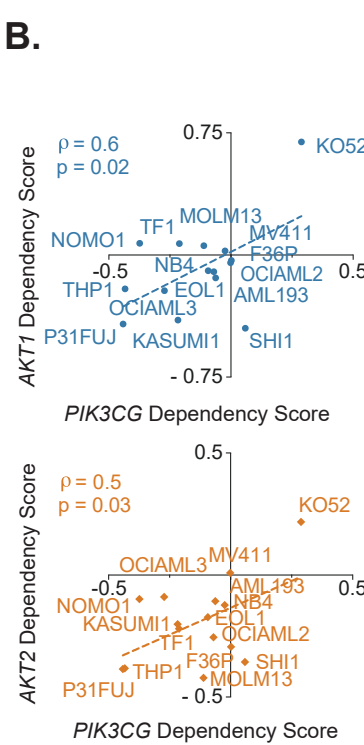
Figure 2

Figure 3

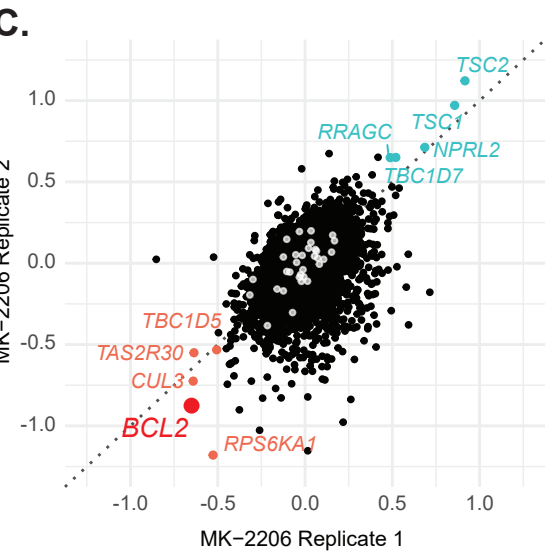
A.



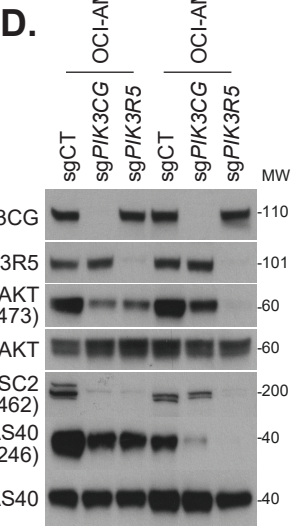
B.



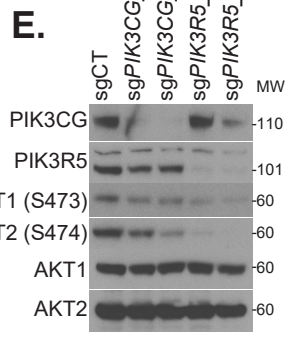
C.



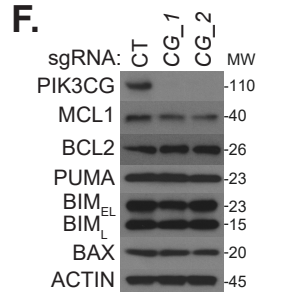
D.



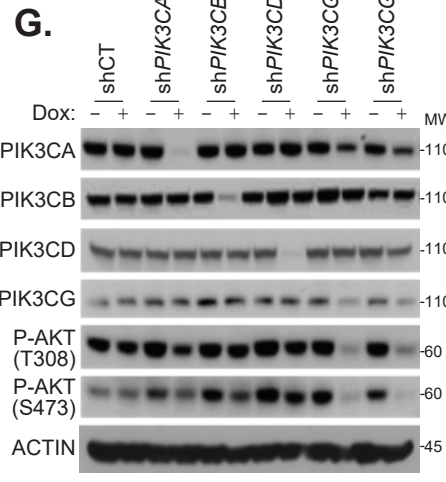
E.



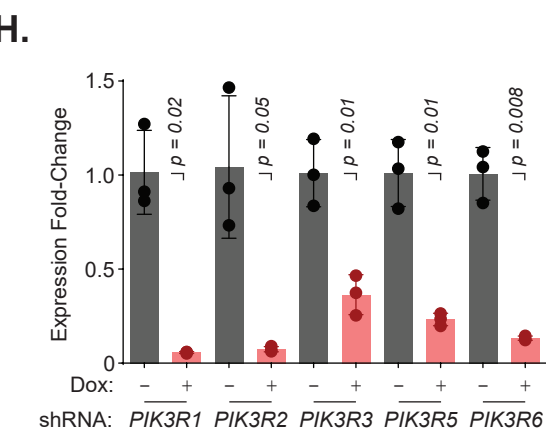
F.



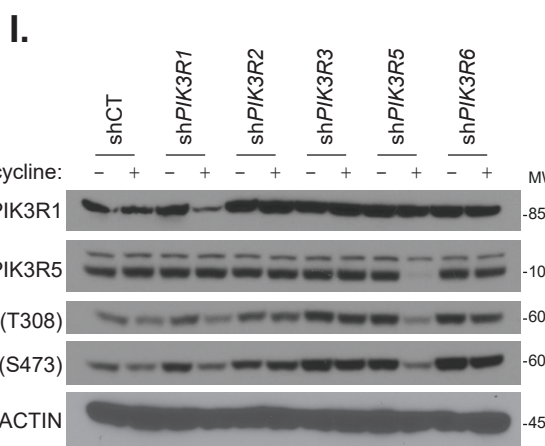
G.



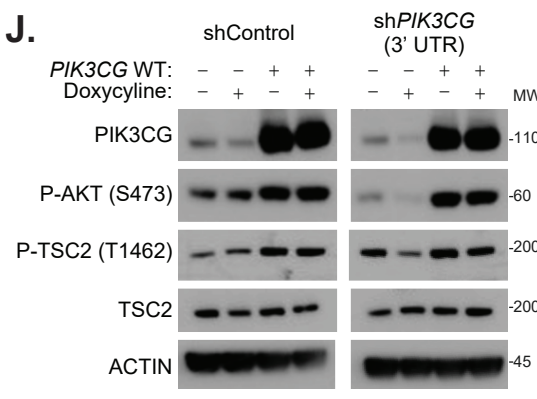
H.



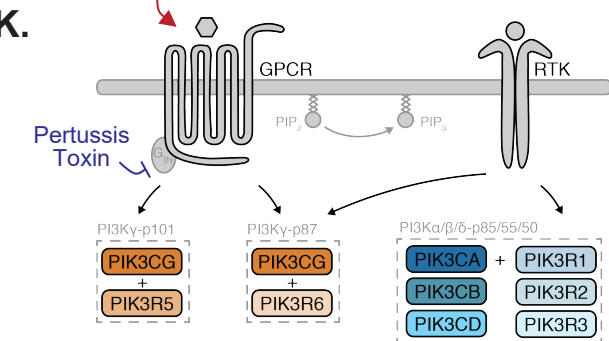
I.



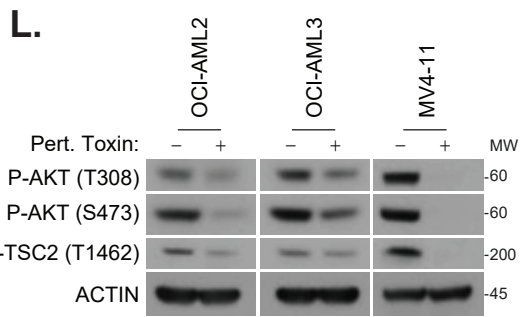
J.



K.



L.



M.

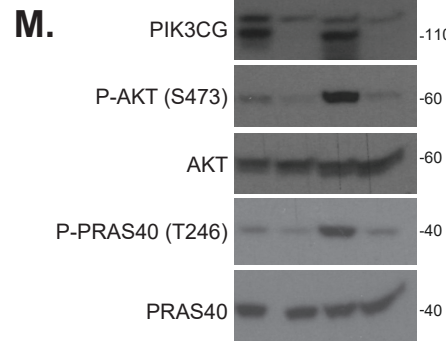


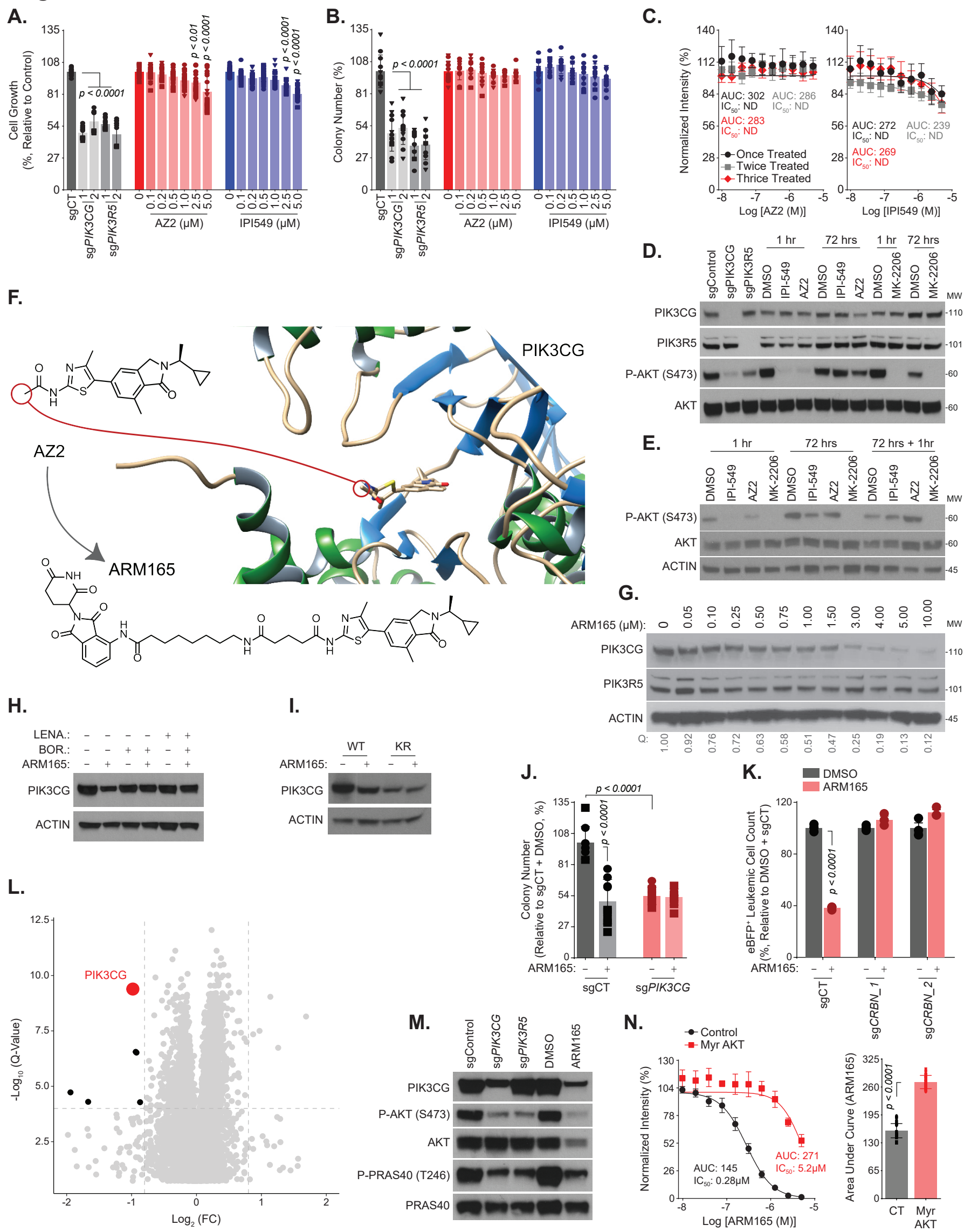
Figure 4

Figure 5

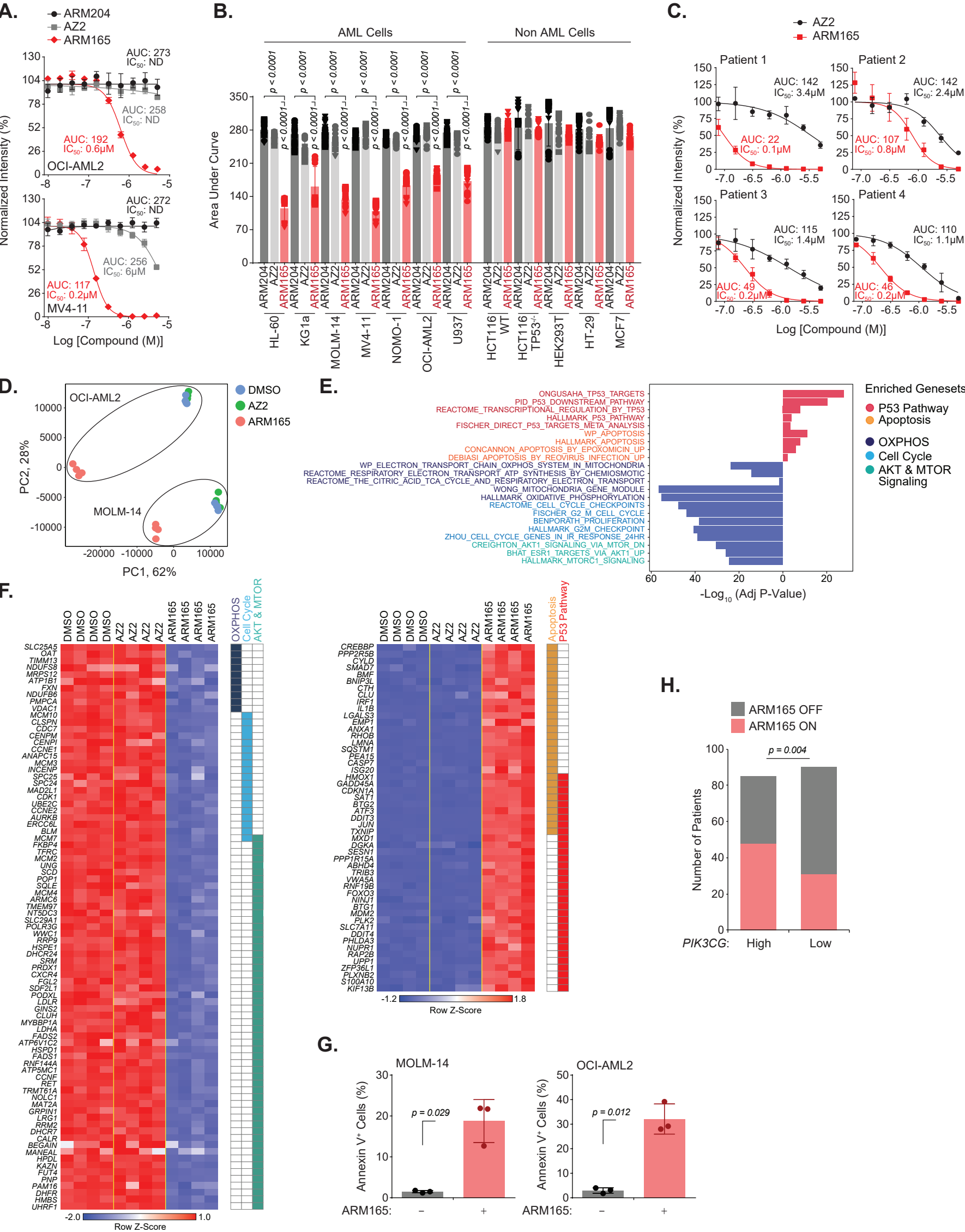
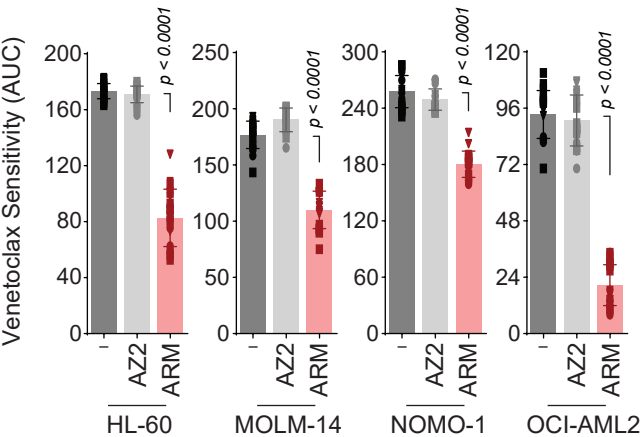
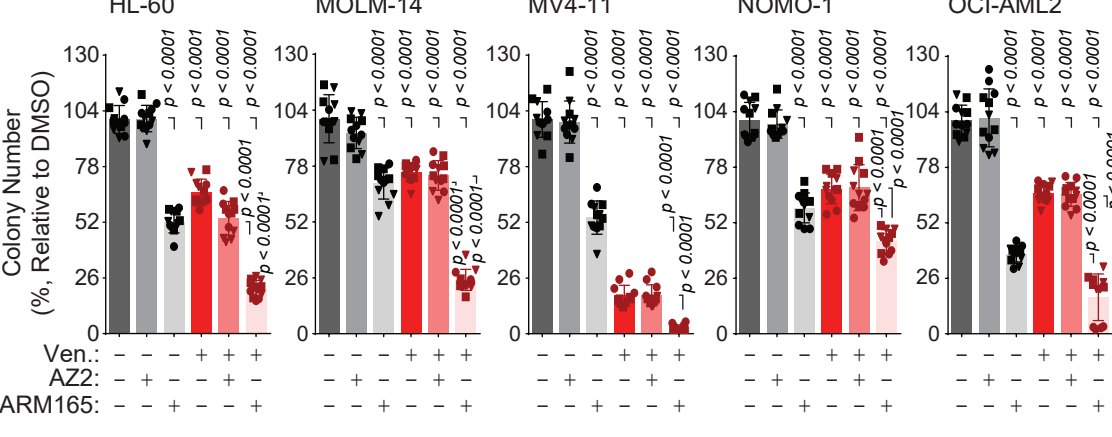


Figure 6

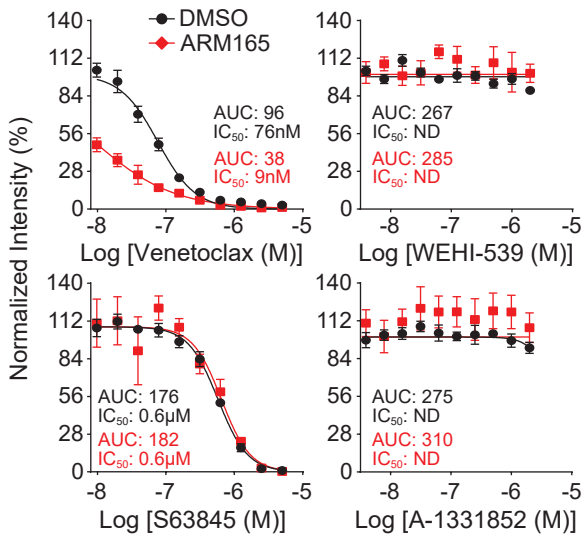
A.



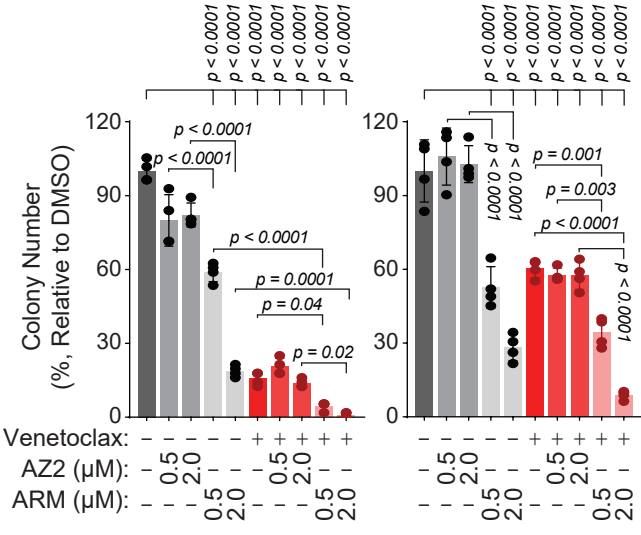
B.



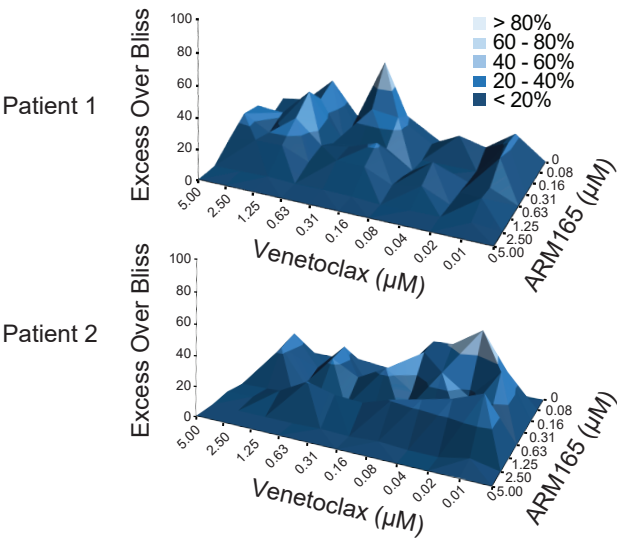
C.



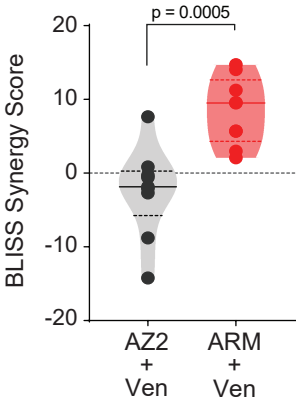
D.



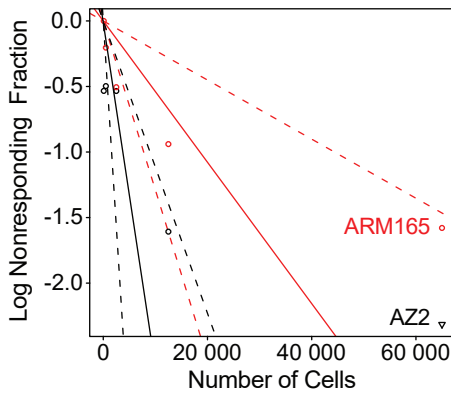
E.



F.

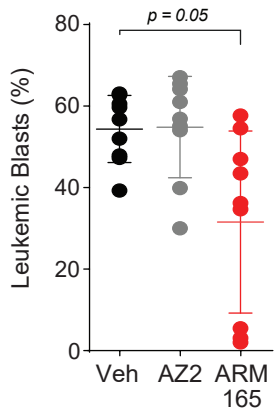


G.

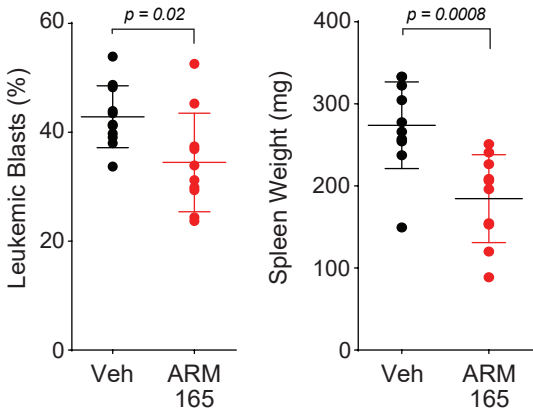


	Demised Mice / Total Mice					LIC Frequency (95% CI)
AZ2	5/5	4/5	2/5	2/5	2/5	1 / 3 785 (1/8 967 - 1/1 598)
ARM165	4/5	3/5	2/5	1/5	0/5	1 / 18 549 (1/44 358 - 1/7 757)
Cell Number	65 000	12 500	2 500	500	100	x 4.9 $\chi^2 = 0.02$

H.



I.



J.

